Journal of the Mechanics and Physics of Solids 145 (2020) 104142

Contents lists available at ScienceDirect

Journal of the Mechanics and Physics of Solids

journal homepage: www.elsevier.com/locate/jmps

A multiscale cohesive zone model for rate-dependent fracture of interfaces

Tianhao Yang, Kenneth M. Liechti, Rui Huang*

Department of Aerospace Engineering and Engineering Mechanics, University of Texas, Austin, TX 78712, USA

ARTICLE INFO

Article history:
Received 12 June 2020
Revised 15 August 2020
Accepted 1 September 2020
Available online 3 September 2020

Keywords:
Interface
Cohesive zone model
Rate-dependent fracture
Freely jointed chain
Bond rupture kinetics

ABSTRACT

Rate-dependent fracture has been observed for a silicon/epoxy interface as well as other polymer interfaces, where both the interfacial strength and toughness increase with the separation rate. Motivated by this observation, we propose a multiscale approach to modeling a polymer interface, from atomic bonds to the macroscopic specimen, considering the energetics of bond stretching, the entropic effect of long molecular chains, the kinetics of thermally activated chain scission, and statistical distributions of the chain lengths. These multiscale features are seamlessly assembled to formulate a rate-dependent cohesive zone model, which is then implemented within a standard finite element package for numerical simulations. This model relates the macroscopically measurable interfacial properties (toughness, strength, and traction-separation relations) to molecular structures of the interface, and the rate dependence results naturally from the kinetics of damage evolution as a thermally activated process. The finite element simulations with the cohesive zone model are directly compared to double cantilever beam experiments for the rate-dependent fracture of a silicon/epoxy interface, yielding reasonable agreement with just a few parameters for the molecular structures of the interface. Such a multiscale, mechanism-based cohesive zone model offers a promising approach for modeling and understanding the rate-dependent fracture of polymer interfaces.

1. Introduction

Rate-dependent fracture of polymers and their interfaces has been commonly observed (de Gennes, 1996; Gent et al., 1969; Knauss, 2015; Kovalchick et al., 2013; Makhecha et al., 2009; Neggers et al., 2015). In practice, the rate-dependent fracture of polymer interfaces has been exploited for transfer printing of microdevices (Meitl et al., 2006) and dry transfer of graphene (Na et al., 2015; Xu et al., 2019). In both cases, an increase in the separation or peeling rate increased the interfacial toughness, although the underlying mechanisms could be different for polymers in rubbery and glassy states. For a polymer in its rubbery state such as PDMS, the rate effect has been attributed to viscoelasticity in the polymer (Chen et al., 2013; Feng et al., 2007). In contrast, for a glassy polymer such as epoxy, since the bulk fracture toughness typically decreases with increasing rate (Makhecha et al., 2009), the increasing toughness for interfacial fracture must be attributed to the rate-dependent interfacial behavior, which is the focus of the present study.

Among various approaches for analyzing interfacial fracture, cohesive zone modeling, first proposed by Barenblatt (1959) and Dugdale (1960), has been widely used as a top-down approach to nonlinear fracture (Hutchinson and

* Corresponding author.
E-mail address: ruihuang@mail.utexas.edu (R. Huang).

https://doi.org/10.1016/j.jmps.2020.104142
0022-5096/

Evans, 2000). The most important aspect in the cohesive zone modeling is to describe the nonlinear fracture processes by a traction-separation relation, which would unambiguously define the key properties of the interface such as toughness and strength. Theoretically, traction–separation relations can be derived from a potential energy function (Xu and Needleman, 1994) or based on various forms of damage evolution (Alfano and Crisfield, 2001; Ungsuwarungsri and Knauss, 1987). Most commonly, however, the traction-separation relation is independent of the separation rate. On the other hand, the traction-separation relations for specific interfaces may be extracted from experiments by either a direct or iterative method (Gowrishankar et al., 2012; Wu et al., 2019). Previous studies have reported a strong rate dependence in the traction-separation relations extracted from experiments for a polyurea/steel interface (Zhu et al., 2009) and for an epoxy/silicon interface (Yang et al., 2019), calling for rate-dependent cohesive zone models.

Various rate-dependent cohesive zone models have been proposed for fracture of polymers and interfaces. A series of papers in the 1990s (Adjari et al., 1994; de Gennes, 1996; Kogan et al., 1996; Raphael and De Gennes, 1992; Xu et al., 1991) proposed a micromechanical model of interfacial deformation and fracture based on the mechanism of chain pull-out, where the traction decreases with the separation and depends on the separation rate. A different approach taken by Knauss and Losi (1993) proposed a model for craze-led crack growth, where a nonlinear viscoelastic constitutive model was assumed in a narrow cohesive zone along the crack plane with an empirical function for damage-induced softening due to void formation. Landis et al. (2000) proposed a cohesive zone model with a viscoplastic traction-separation relation along with a micromechanical void cell model to predict the macroscopic toughness as a function of the crack velocity for quasi-static, steady-state crack growth in rate-dependent (viscoplastic) materials. Liechti and Wu (2001) used a nonlinear viscoelastic Kelvin element to simulate the rate-dependent cohesive forces between rubber and steel under mixed-mode loading at different rates. A similar approach was followed by Xu et al. (2003) in a rate-dependent cohesive zone model consisting of a viscoelastic Maxwell element in parallel to a nonlinear spring. A more sophisticated model was proposed by Zhang et al. (2003) with a cohesive zone consisting of a plastic region and a damage region, each following a rate-dependent traction-separation relation. Many other works have simply extended the rate-independent cohesive zone models by using rate-dependent parameters in the traction-separation relations without referring to specific mechanisms (Makhecha et al., 2009; Marzi et al., 2009; Mohammed et al., 2016).

Yet another mechanism for rate-dependent fracture has been proposed based on thermally activated kinetic bond rupture processes. Following Zhurkov (1965), a kinetic theory of bond dissociation and formation was adopted by Bell (1978) for the study of cell adhesion. As noted by Evans and Ritchie (1997), Bell's model is an extension of the classical transition state theory, which has been followed by many. Notably, Ghatak et al. (2000) extended the kinetic theory to the study of rate-dependent adhesion and friction. A modified version of Bell's model was used to describe interactions between epoxy and silica (Büyüköztürk et al., 2011). Wei (2014) proposed a stochastic interface model with the bonding probability following the Boltzmann distribution in the static case and a kinetic rate equation in the dynamic case. However, it was found that the classical transition-state theory always overestimates the true rate (Hänggi et al., 1990), while the reaction-rate theory originally proposed by Kramers (1940) offers a more accurate description of the kinetics by considering a diffusion process of the energy state. Building on the work of Kramers (1940), Freund (2009) established the dependence of force history of a molecular bond on the controllable loading parameters, leading to an explicit expression for the time-dependent off-rate for bond rupture. This kinetic model was later extended to a study on the growth of a planar crack in a brittle material (Freund, 2014), with a cohesive zone spanned by a large number of identical bonds. By describing the collective response of these bonds in terms of the behavior of a generic bond and the statistical concept of bond survival probability, the traction-separation process in the cohesive zone can be followed to its end without the additional requirement of a failure criterion. A similar model was proposed by Qian et al. (2017) to describe thermally assisted peeling of an elastic strip adhered to a flat substrate with a bond-mediated interface, predicting a strongly rate-dependent behavior in terms of the apparent adhesion strength and energy.

In a recent study (Yang et al., 2019), the rate-dependent fracture of an epoxy/silicon interface was established by double cantilever beam experiments that motivated a rate-dependent cohesive zone model based on the thermally activated bond rupture mechanism. Two key assumptions were made: (1) the bond force is a linear function of the separation, and (2) the energy barrier for bond rupture is a linear function of the bond force. While the previous model could predict rate-dependent traction-separation relations and was able to reproduce the experimental results with a few model parameters, the underlying molecular structures were not considered. Moreover, the assumptions on the linear bond force and the energy barrier should be relaxed by considering specific deformation and fracture mechanisms at the molecular level.

In this paper, we propose a bottom-up multiscale approach to modeling rate-dependent interfacial fracture processes consisting of four levels (Fig. 1), namely, the bond level (Section 2), the chain level (Sections 3 and 4), the interface level (Sections 5 and 6), and finally the specimen level (Section 7). Each level can be considered independently with various modeling candidates (e.g., different bond or chain models) and then integrated with the other levels. Ultimately, such a multiscale interface model links the macroscopic description of the interfacial fracture to the underlying molecular mechanisms. Once calibrated, such a model could be predictive of the interfacial behaviors under various loading conditions. To illustrate the multiscale approach, we adopt the generic Lennard-Jones potential at the bond level, a modified version of the freely jointed chain model at the chain level, and a normal (Gaussian) distribution for the chain lengths at the interface level, along with a kinetic model for damage evolution based on the thermally activated chain scission mechanism. The resulting interface model is implemented as a user-defined module (user subroutine, UINTER) in the commercial finite element package ABAQUS to simulate the rate-dependent fracture of an epoxy/silicon interface at the specimen level, allowing

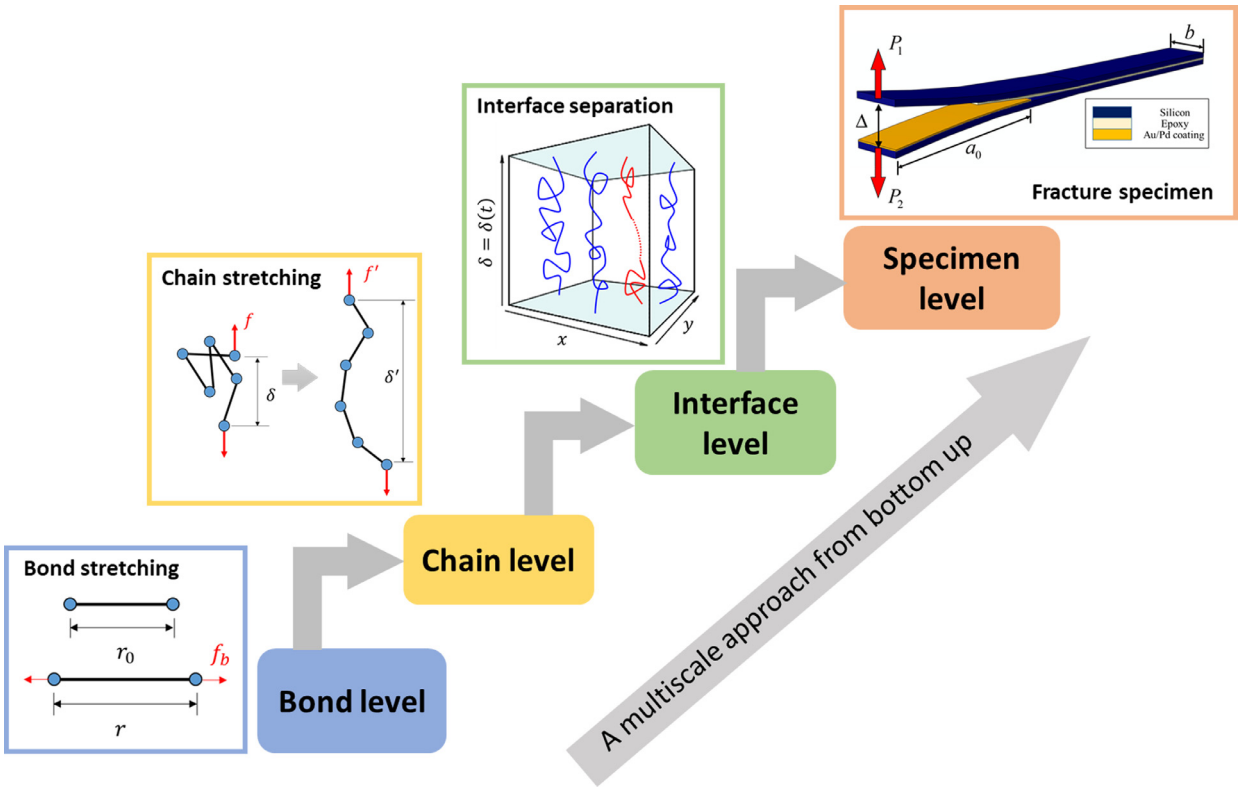

Fig. 1. Illustration of a multiscale approach with four levels of modeling for a polymeric interface.

direct comparison with the double cantilever beam experiments and extraction of the model parameters for the specific interface.

2. Bond stretching

As a bottom-up multiscale approach (Fig. 1), we start at the bond level by modeling the bond stretching between two atoms (or clusters), characterized by a minimum of two parameters: the equilibrium bond length r_0 and the bond energy ε_0. When the bond is stretched to an arbitrary length r, the potential energy of the bond (U_b) can be written as a function of the bond stretch, $\lambda_b = r/r_0$. For example, the well-known Lennard-Jones (LJ) potential function can be written as

$$U_b(\lambda_b) = \varepsilon_0\left(\lambda_b^{-12} - 2\lambda_b^{-6}\right). \tag{2.1}$$

The interaction force between the two atoms can be obtained from the potential energy function as $f_b = \frac{\partial U_b}{\partial r}$, which can also be written as a function of the bond stretch. Using the LJ potential, we obtain

$$f_b(\lambda_b) = \frac{12\varepsilon_0}{r_0}\left(\lambda_b^{-7} - \lambda_b^{-13}\right). \tag{2.2}$$

When the bond is slightly stretched, the potential energy is often approximated by a quadratic function assuming a linear spring constant as the bond stiffness. With the same bond stiffness as the LJ potential at $\lambda_b = 1$, the approximate potential energy is:

$$U_b(\lambda_b) \approx \varepsilon_0\left[36(\lambda_b - 1)^2 - 1\right], \tag{2.3}$$

and the corresponding bond force is linear:

$$f_b(\lambda_b) \approx \frac{72\varepsilon_0}{r_0}(\lambda_b - 1). \tag{2.4}$$

A slightly different approximation was recently suggested by Mao et al. (2017), where the potential energy is taken as a quadratic function of the logarithmic strain (namely, a logarithmic spring model):

$$U_b(\lambda_b) \approx \varepsilon_0\left[36(\ln\lambda_b)^2 - 1\right], \tag{2.5}$$

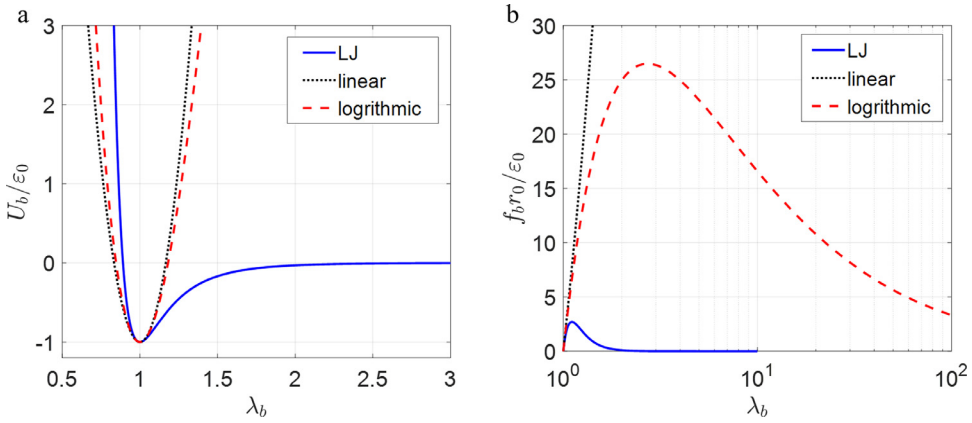

Fig. 2. Comparison of the LJ potential and two approximations: (a) the potential energy; (b) the bond force.

and the corresponding bond force is nonlinear:

$$f_b(\lambda_b) \approx \frac{72\varepsilon_0}{r_0}\frac{\ln\lambda_b}{\lambda_b}. \tag{2.6}$$

In Fig. 2, we compare the LJ potential and the two approximations, where the normalized bond energy ($\bar{U}_b = U_b/\varepsilon_0$) and force ($\bar{f}_b = f_b r_0/\varepsilon_0$) are plotted versus the bond stretch. The LJ potential has three key features that are common for essentially all types of bonds: (1) the potential energy is minimized at an equilibrium bond length ($r = r_0$ or $\lambda_b = 1$); (2) the potential energy becomes infinitely high as the two atoms approach each other ($r \to 0$); (3) the potential energy approaches zero as the two atoms are separated far apart from each other ($r \to \infty$). As a result, the corresponding bond force first increases and then decreases toward zero as the bond stretch increases, and the work done by the force to break the bond equals the bond energy ε_0. The linear spring approximation has only one of the three features and is valid only near the equilibrium state ($r \approx r_0$ or $\lambda_b \approx 1$), thus not suitable for the study of bond rupture. On the other hand, the logarithmic spring approximation retains the first two features, but the potential energy is unbounded as $r \to \infty$. Interestingly, the bond force derived from the logarithmic spring model does approach zero as $r \to \infty$, but with a much higher peak force (at $\lambda_b = e$) and much slower softening in comparison to the bond force by the LJ potential. In view of its simplicity, we use the LJ potential in this work as a generic bond model with all three key features, although other potential functions can be used as well.

3. Chain stretching: a modified freely jointed chain model

Next consider a chain of bonds. Following the freely jointed chain (FJC) theory (Kuhn and Grün, 1942), the free energy of a single chain with n bonds[1] is

$$\psi = nk_BT\left(\frac{l}{nr_0}\beta + \ln\left(\frac{\beta}{\sinh\beta}\right)\right) \tag{3.1}$$

where $\beta = \mathcal{L}^{-1}(\frac{l}{nr_0})$ and $\mathcal{L}^{-1}$ is the inverse Langevin function; l denotes the average end-to-end distance of the chain, $k_B = 1.38 \times 10^{-23}$J/K (Boltzmann constant), and T is temperature. The classical FJC model assumes that each bond is a rigid link of length r_0 (Kuhn segment) so that the free energy is entirely entropic. To account for the bond stretch that may lead to bond rupture, we follow (Mao et al., 2017) to extend the FJC model by relaxing the rigid-bond assumption and replacing r_0 with $r = \lambda_b r_0$, where λ_b is the bond stretch. In addition, the internal energy associated with the bond stretching is included as part of the free energy function so that the free energy of the modified FJC model is

$$\psi = nU_b(\lambda_b) + nk_BT\left(\frac{\lambda}{\lambda_b}\beta + \ln\left(\frac{\beta}{\sinh\beta}\right)\right) \tag{3.2}$$

where $\beta = \mathcal{L}^{-1}(\frac{\lambda}{\lambda_b})$ and $\lambda = \frac{l}{nr_0}$ (called chain stretch hereafter). Eq. (3.2) recovers Eq. (3.1) if $\lambda_b \equiv 1$ (rigid bonds) except for a constant internal energy term.

[1] In polymer physics literature, the unit of a freely jointed chain is often referred to as a Kuhn segment. Each Kuhn segment may consist of several bonds (Lavoie et al., 2020). Here we treat each Kuhn segment as one bond following Eq. (2.2) as a specific force-extension relationship.

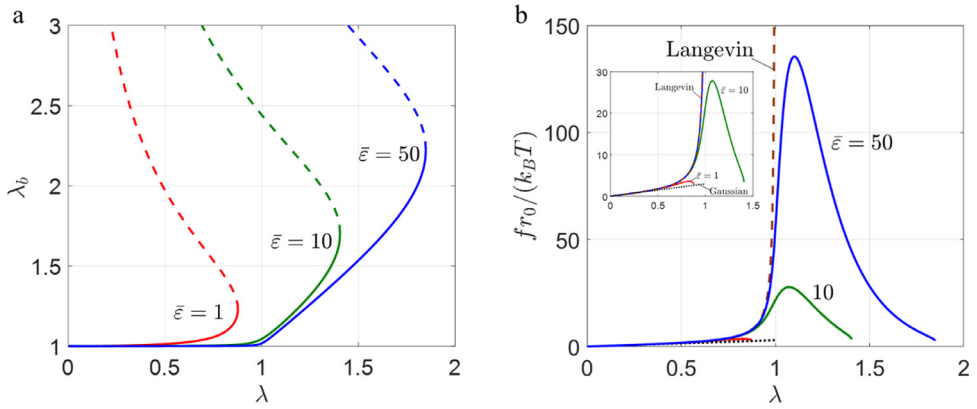

Fig. 3. Modified FJC model with the LJ potential for the bonds: (a) equilibrium bond stretch versus chain stretch, and (b) end force versus chain stretch. Inset shows the linear Gaussian behavior at small stretches.

At a prescribed chain stretch λ, the bond stretch λ_b is determined by minimizing the free energy in Eq. (3.2) as the equilibrium state. Thus, by setting $\frac{\partial \psi}{\partial \lambda_b} = 0$, we obtain

$$\frac{1}{k_B T}\frac{dU_b}{d\lambda_b} = \frac{\lambda}{\lambda_b^2}\mathcal{L}^{-1}\left(\frac{\lambda}{\lambda_b}\right), \tag{3.3}$$

which yields λ_b as a function of λ. As a result, the free energy of the chain is a function of the chain stretch, namely, $\psi = \psi(\lambda)$. Then, to maintain the chain stretch λ, the force applied at the ends of the chain can be obtained as

$$f = \frac{1}{nr_0}\frac{d\psi}{d\lambda} = \frac{k_B T}{\lambda_b r_0}\mathcal{L}^{-1}\left(\frac{\lambda}{\lambda_b}\right). \tag{3.4}$$

We note that, by Eqs. (3.3) and (3.4), the chain force and the bond force are related as: $f = \frac{\lambda_b}{\lambda r_0}\frac{dU_b}{d\lambda_b} = \frac{\lambda_b}{\lambda} f_b$, or $f\lambda = f_b\lambda_b$. It can be seen that $\beta = \frac{\lambda_b r_0}{k_B T} f$, which is essentially the same in the classical FJC model except for the stretched bond length ($\lambda_b r_0$).

To illustrate the modified FJC model, we use the LJ potential (Eq. (2.1)) for the bonds and calculate the bond stretch (λ_b) as a function of the chain stretch (λ) by Eq. (3.3) for different values of the normalized bond energy ($\bar{\varepsilon} = \frac{\varepsilon_0}{k_B T}$), as shown in Fig. 3a. Correspondingly, the normalized end force ($\bar{f} = \frac{f r_0}{k_B T}$) applied to the chain is calculated by Eq. (3.4) as shown in Fig. 3b. When the normalized bond energy is relatively high (e.g., $\bar{\varepsilon} = 50$), the bond stretch remains nearly 1 (un-stretched) until the chain stretch reaches 1, similar to the classical FJC model. However, unlike the classical FJC model where the chain stretch λ must be always less than 1 with $\lambda_b \equiv 1$ (rigid bonds), the modified FJC model allows the chain stretch λ to be greater than 1 as the bond stretch increases almost linearly when $\lambda > 1$ for the case of $\bar{\varepsilon} = 50$. Correspondingly, the normalized force first increases slowly for $\lambda < 1$, primarily due to the entropic effect. As λ approaches 1, the chain stiffens and transitions to a response primarily due to the bond stretch, with a peak force ($f_{\max}$) followed by softening as a result of the LJ potential. When the normalized bond energy is relatively low (e.g., $\bar{\varepsilon} = 10$), the overall behavior is similar, but the bond stretch is larger at the same chain stretch. Interestingly, there exists a critical chain stretch ($\lambda_{\max}$), beyond which the free energy cannot be minimized by any value of the bond stretch. The critical chain stretch decreases as the normalized bond energy decreases and could be less than 1 for a very low bond energy (e.g., $\bar{\varepsilon} = 1$). In such cases, the bonds can be easily stretched (i.e., soft bonds), and the increase of the bond energy is small compared to the decrease of the entropic free energy. The competition between the two parts of the free energy (bond stretching vs entropy) also leads to an unstable solution for the bond stretch shown by the dashed lines in Fig. 3a, where the free energy is locally maximized.

We compare the modified FJC model to two classical chain models, Gaussian and Langevin, both purely entropic with no contribution from bond stretching. The Gaussian chain model predicts a linear response, $\bar{f} = 3\lambda$, shown as the dotted line in Fig. 3b. Independent of the normalized bond energy, the predictions by the modified FJC model agree with the Gaussian model when the chain stretch is very small ($\lambda \ll 1$). On the other hand, the Langevin model (i.e., the classical FJC model) predicts a nonlinear response with a limiting stretch ($\lambda < 1$): $\bar{f} = \mathcal{L}^{-1}(\lambda)$, shown as the dashed line in Fig. 3b. The modified FTC model would recover the Langevin model if the normalized bond energy is infinitely large ($\bar{\varepsilon} \to \infty$). For a relatively large bond energy ($\bar{\varepsilon} = 50$), the modified FJC model is similar to the Langevin model when $\lambda < 1$, but the chain can be stretched further by increasing bond stretch. For $\lambda > 1$, the chain behavior is dominated by bond stretching, with $\bar{f} \approx 12\bar{\varepsilon}(\lambda^{-7} - \lambda^{-13})$ following the LJ potential. Thus, the modified FJC model predicts a transition from Langevin to LJ. When the bond energy is relatively small ($\bar{\varepsilon} = 1,\ 10$), the effect of bond stretching competes with the entropic effects even at small stretches ($\lambda < 1$),

leading to more compliant chain responses along with a lower peak force ($f_{\max}$) and a smaller maximum chain stretch ($\lambda_{\max}$).

4. Energy barrier for chain scission

Previous studies have considered the kinetics of thermally activated bond rupture in various materials and interfaces (Bell, 1978; Freund, 2014; Yang et al., 2019; Zhurkov, 1965). Following a similar idea, we consider the kinetics of thermally activated chain scission at the interface level (Section 5), which requires determination of an energy barrier based on the energetics at the chain level.

In Section 3 we have assumed the same stretch for all bonds in a freely jointed chain as the equilibrium state. For chain scission, however, only one bond may be broken while the other bonds return to the unstretched state. The transition from an equilibrium state of the chain to the state of a broken chain (with one broken bond) may be traversed along a path with the minimum energy barrier in the energy landscape. In general, such an energy landscape may include states with various bond stretches, where one of the bonds may be stretched the most and hence most likely to break. To find the path with the minimum energy barrier, we consider a freely jointed chain with n bonds, each stretched by an arbitrary amount, λ_{bi} ($i = 1, 2, \ldots, n$). The statisticaly averaged end-to-end distance of the chain is then:

$$l = \sum_{i=1}^{n} \lambda_{bi} r_0 \mathcal{L}(\beta_i), \tag{4.1}$$

where $\beta_i = \lambda_{bi} \frac{f r_0}{k_B T}$. Including the potential energy of the variously stretched bonds, the total free energy of the chain is:

$$\psi = \sum_{i=1}^{n} \left[U_b(\lambda_{bi}) + k_B T \left(\beta_i \mathcal{L}(\beta_i) + \ln \frac{\beta_i}{\sinh(\beta_i)} \right) \right]. \tag{4.2}$$

For a chain subject to an external force f, the Gibbs free energy of the system including the chain and the external force is:

$$\phi(\lambda_{bi}) = \psi - fl = \sum_{i=1}^{n} \left[U_b(\lambda_{bi}) + k_B T \ln \frac{\beta_i}{\sinh(\beta_i)} \right]. \tag{4.3}$$

By minimizing the free energy in Eq. (4.3) with respect to each bond stretch, we obtain

$$\frac{\partial \phi}{\partial \lambda_{bi}} = U_b'(\lambda_{bi}) - k_B T \bar{f} \mathcal{L}\left(\lambda_{bi} \bar{f}\right) = 0, \tag{4.4}$$

which can be solved to determine the bond stretch λ_{bi} as a function of the force f (recall that $\bar{f} = \frac{f r_0}{k_B T}$). Using the LJ potential for the bond energy, we obtain

$$12\bar{\varepsilon}\left(\lambda_{bi}^{-7} - \lambda_{bi}^{-13}\right) - \bar{f}\mathcal{L}\left(\lambda_{bi}\bar{f}\right) = 0, \tag{4.5}$$

where $\bar{\varepsilon} = \frac{\varepsilon_0}{k_B T}$ is the normalized bond energy. Solving the above equation, we obtain the same bond stretch for all bonds, namely, $\lambda_{bi} = \lambda_b^e(\bar{f}, \bar{\varepsilon})$.

For a given force and a bond energy, the free energy landscape by Eq. (4.3) is n-dimensional with a local minimum (or maximum) when all bonds are equally stretched, which corresponds to the equilibrium state of the chain as discussed in Section 3. For one of the bonds to break, we follow a path with all the bonds stretched by the equilibrium stretch $\lambda_b^e(\bar{f}, \bar{\varepsilon})$ except for one bond with a varying stretch, λ_{b^*}. The choice of the particular bond does not matter because the trajectory in the energy landscape is identical. Along this path, the free energy is a function of the varying bond stretch (λ_{b^*}), namely

$$\phi(\lambda_{b*}) = \left(1 - \frac{1}{n}\right)\phi_m + \phi^*(\lambda_{b*}), \tag{4.6}$$

where $\phi_m = n[U_b(\lambda_b^e) + k_B T \ln \frac{\lambda_b^e \bar{f}}{\sinh(\lambda_b^e \bar{f})}]$ is the local minimum (or maximum) free energy with all bonds at the equilibrium stretch ($\lambda_{bi} = \lambda_b^e$) and

$$\phi^*(\lambda_{b*}) = U_b(\lambda_{b*}) + k_B T \ln \frac{\lambda_{b*}\bar{f}}{\sinh\left(\lambda_{b*}\bar{f}\right)}. \tag{4.7}$$

Fig. 4a shows that, for $0 < \bar{f} < \bar{f}_{max}$, the free energy has a local minimum at $\lambda_{b*} = \lambda_b^e$ (the equilibrium state of the chain) and a local maximum at $\lambda_{b*} = \lambda_{b^\wedge}(\bar{f}, \bar{\varepsilon}_0)$. Beyond the local maximum, the free energy decreases as λ_{b^*} increases, approaching the state of a broken chain with $\lambda_{b^*} \to \infty$. The local maximum in Fig. 4a is actually a saddle point (transition state) in the n-dimensional energy landscape, $\phi(\lambda_{bi}; i = 1, 2, \ldots, n)$, since the free energy is locally minimized with respect to the other bond stretches. Hence, the energy barrier for one of the bonds to break is:

$$E_b = \phi^*(\lambda_{b^\wedge}) - \phi^*\left(\lambda_b^e\right), \tag{4.8}$$

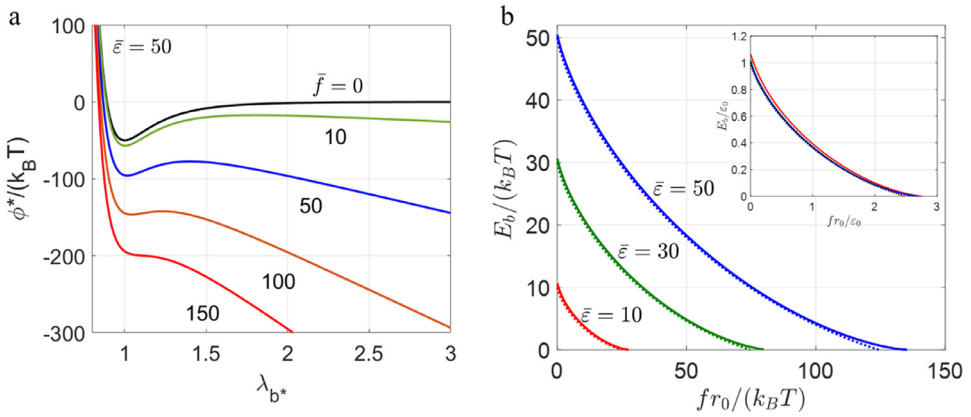

Fig. 4. (a) Normalized free energy ($\bar{\varepsilon} = 50$) subject to various forces; (b) Normalized energy barrier as a function of the normalized force at various values of the normalized bond energy. The inset shows the energy barrier normalized by the bond energy versus the force normalized by ε_0/r_0.

which is a function of the applied force as shown in Fig. 4b. It is noted that, in the n-dimensional energy landscape, there exist n different paths (one for each bond) with the same energy barrier, through which the state of the chain transitions from the same equilibrium state to the states with one broken bond. The energy barrier is independent of the chain length (n).

As expected, the energy barrier decreases as the force increases (Fig. 4b). The action of an external force lowers the energy barrier, making the chain less stable and more likely to break. At zero force ($\bar{f} = 0$), the energy barrier approximately equals the bond energy. For a given bond energy, the energy barrier becomes zero at $\bar{f} = \bar{f}_{\max}$, when chain scission occurs instantaneously. For $\bar{f} \geq \bar{f}_{\max}$, the free energy decreases monotonically with increasing λ_{b^*}, with no local minimum for an equilibrium stretch. Therefore, the maximum force defines an ultimate strength of the chain (see Fig. 3b). We note that both the energy barrier and the maximum force are nearly proportional to the bond energy (ε_0), as shown by replotting in the inset of Fig. 4b with the energy barrier and the force re-normalized using ε_0 (instead of $k_B T$). The results for various bond energy values almost collapse onto one curve, with small differences for relatively low bond energy (e.g., $\bar{\varepsilon} = 10$) due to the entropic contribution in the free energy function.

Following the kinetic theory for the strength of solids (Zhurkov, 1965), Bell (1978) assumed that the energy barrier for bond breaking decreases linearly with the applied force: $E_b = \varepsilon_0 - \gamma f$, where γ is an empirical parameter ($\gamma \sim \varepsilon_0/f_{max}$). A similar assumption has been commonly adopted in previous works (Ackbarow et al., 2007; Chaudhury, 1999; Ghatak et al., 2000; Pobelov et al., 2017; Wiita et al., 2006; Yang et al., 2019). However, Fig. 4b shows that the energy barrier is a nonlinear function of the force in the present model. By ignoring the entropic effect, an approximate expression for the energy barrier can be obtained as

$$E_b \approx \varepsilon_0 \left(1 - 1.664 \hat{f}^{6/7} + \hat{f} + 0.0236 \hat{f}^2\right), \tag{4.9}$$

where $\hat{f} = \frac{f r_0}{\varepsilon_0}$. This approximation is shown as the dotted lines in Fig. 4b with excellent agreement with those calculated by Eq. (4.8). Note that the leading term on the right-hand side (after the constant term) of Eq. (4.9) is nonlinear ($\sim \hat{f}^{6/7}$), with an infinite slope at $\hat{f} = 0$. Thus, even for a small force ($\hat{f} \ll 1$), the linear approximation is not justified by this model.

The above discussion of the energy barrier assumes that the chain is subject to a constant force (force control). Alternatively, if the chain is subject to a constant stretch λ by displacement-controlled stretching, the energy landscape could be different. In this case, the free energy in Eq. (4.2) is minimized with Eq. (4.1) as a constraint at the equilibrium state. Again, the same equilibrium state is obtained for $\lambda < \lambda_{max}$ (Fig. 3a), with all bonds equally stretched. To find the energy barrier as a function of the chain stretch λ, we follow a similar path in the n-dimensional energy landscape with one bond stretched differently from the others. It is found that the energy barrier decreases with increasing chain stretch and approaches zero when the chain stretch approaches the value corresponding to the maximum force ($\bar{f}_{\max}$ in Fig. 3b), beyond which the local minimum of the energy landscape becomes a local maximum and thus the equilibrium state with all bonds equally stretched becomes unstable (and hence inaccessible). As a result, the chain would break instantaneously once the maximum force (f_{max}) is reached, even under displacement control. In fact, the energy barrier is nearly identical to that calculated under force control as long as $n \gg 1$. In such cases ($n \gg 1$), the change in one bond stretch (up to the point of local maximum ($\lambda_{b^\wedge}$) has a negligible effect on the total chain stretch and the chain force, hence essentially no difference in terms of the energy barrier between the force-controlled and the displacement-controlled conditions. Therefore, the same energy barrier (Eq. (4.9)) can be used under either condition for a long chain ($n \gg 1$).

We note one subtle difference between force-controlled and displacement-controlled stretching. Under force control, all bonds are subject to the same force and the free energy decreases indefinitely as $\lambda_{b^*} \to \infty$ (Fig. 4a), hence there is no absolute energy minimum under a constant force ($\bar{f} > 0$). In contrast, under displacement control, the force changes as

λ_{b^*} changes and eventually approaches zero as $\lambda_{b^*} \to \infty$. Meanwhile, the free energy approaches another local minimum, $\psi \to -(n-1)\varepsilon_0$, corresponding to the state of a broken chain with one bond broken and all other bonds fully relaxed ($\lambda_b = 1$). In such a case, it is possible to calculate the energy barrier for the inverse transition from the broken chain to a continuous chain (i.e., healing), which would decrease as the chain stretch (λ) decreases. Therefore, under displacement control, the state of a chain could go both ways, with two different energy barriers. In the present work, we focus on chain scission and ignore the possibility of chain healing.

5. Interface level: Thermally activated damage evolution

Now consider the kinetics of chain scission at the interface level with a large number of chains. As noted by Freund (2014), the statistics of bond breaking for a large number of nominally identical bonds can be interpreted equivalently as the survival probability of each single bond. The bond survival probability then follows the Arrhenius law as a result of the thermally activated bond breaking process (Yang et al., 2019), namely

$$\frac{\dot{R}_b}{R_b} = -\frac{1}{t_0}\exp\left(-\frac{E_b}{k_B T}\right), \tag{5.1}$$

where $\dot{R}_b = dR_b/dt$ is the rate of the bond survival probability (R_b), E_b is the energy barrier for bond rupture, and t_0 is a microscopic time scale. The right hand side of Eq. (5.1) is often called bond dissociation (off) rate (Bell, 1978; Freund, 2014). The time scale t_0 is often taken as the reciprocal of the natural frequency of atomic oscillation (attempt frequency), i.e., $t_0 = \frac{\hbar}{k_B T} \sim 10^{-13}$s, following classical transition-state theory (Makarov, 2015), although different time scales have been suggested by others (Hänggi et al., 1990; Makarov, 2015).

For a chain of n identical bonds, the survival probability of the chain is related to the survival probability of each bond as

$$R_{chain} = R_b^n \tag{5.2}$$

because the chain survives only if all the bonds survive. Thus, the rate equation for the chain survival probability is:

$$\frac{\dot{R}_{chain}}{R_{chain}} = -\frac{n}{t_0}\exp\left(-\frac{E_b}{k_B T}\right) \tag{5.3}$$

Compared to the bond survival probability, the chain survival probability also depends on the chain length (n). The longer the chain, the more likely it is to break under the same thermomechanical conditions. Eq. (5.3) can also be understood in terms of the n-dimensional energy landscape as discussed in Section 4, where n different paths exist for the transition from a local minimum (the equilibrium state) to one of the n states, each with one broken bond. With an energy barrier (E_b) for such transition paths as determined in Section 4 (e.g., Fig. 4b or Eq. (4.9)), the survival probability of the chain follows the rate equation in Eq. (5.3). We note that the energy barrier normalized by the thermal energy ($k_B T$) determines the rate of chain scission and hence the survival probability. When the applied force is small, the energy barrier is high and the chain scission is unlikely within a short time (e.g., an experimental time scale). As the applied force increases, the energy barrier decreases (Fig. 4b) and chain scission becomes more likely within the same time scale. When the force is equal to or greater than the maximum force ($f \geq f_{\max}$), the energy barrier is zero so that the chain scission rate is extremely high (similar to atomic oscillations) and the chain breaks almost instantaneously. As noted in Section 4, healing is possible under displacement control, which would add a positive term to the right hand side of Eq. (5.3) if considered.

If an interface consists of a large number of nominally identical chains and is subject to an opening traction (force per unit area of the interface), $\sigma(t)$, some of the chains may have been broken while the others remain intact at a given time. Let $N(t)$ be the number of intact chains per unit area of the interface and $N_0 = N(t=0)$ be the initial number density. Define the damage of the interface as:

$$D(t) = 1 - \frac{N(t)}{N_0} = 1 - R_{chain}(t). \tag{5.4}$$

Then, following Eq. (5.3), the rate equation for damage evolution of the interface is:

$$\frac{dD}{dt} = \frac{n}{t_0}(1-D)\exp\left(-\frac{E_b}{k_B T}\right). \tag{5.5}$$

At any given time, each of the intact chains is subject to a force, $f = \sigma/N$. Thus, the traction can be related to the damage parameter as

$$\sigma = (1-D)N_0 f, \tag{5.6}$$

where the force f can be related to the chain stretch λ (see Fig. 3b) by the modified FJC model and the chain stretch is related to the opening separation of the interface as:

$$\delta = \lambda n r_0. \tag{5.7}$$

Therefore, with Eq. (3.4) for the force-stretch relation of a chain, Eq. (4.9) for the energy barrier, Eq. (5.5) for damage evolution, Eq. (5.6) for the traction, and Eq. (5.7) for the separation, we obtain a traction-separation relation for the interface,

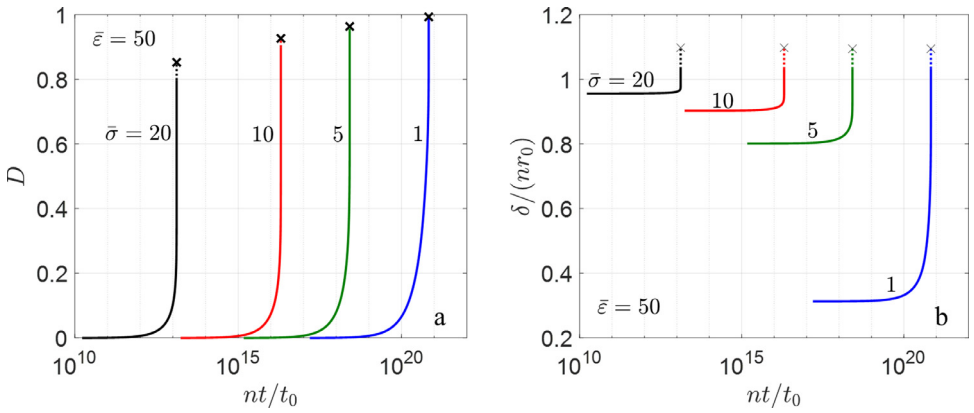

Fig. 5. (a) Damage evolution and (b) normalized separation over time under constant tractions for $\bar{\varepsilon} = 50$.

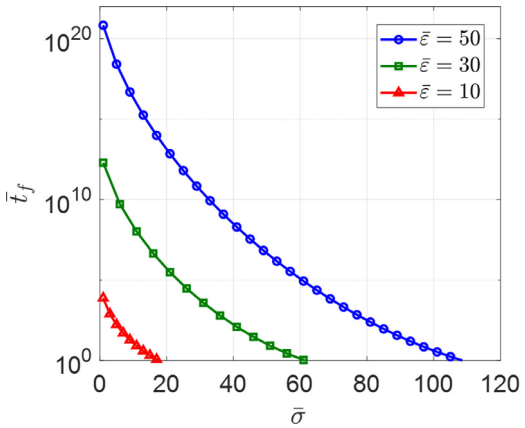

Fig. 6. Predicted time to failure versus the normalized traction for different values of $\bar{\varepsilon}$.

which is inherently time dependent, rate dependent and history dependent due to thermally activated chain scission as the underlying mechanism for the interfacial damage evolution. Remarkably, such an interface model directly links the traction-separation relation at the interface level to the molecular structures in terms of the initial chain number density (N_0), the chain length (n) and the bond properties (r_0 and ε_0). Moreover, the thermally activated chain scission mechanism naturally depends on temperature through both the energetics (k_BT versus E_b) and the kinetics ($t_0 = \frac{\hbar}{k_BT}$). The effect of entropy is also accounted for through the modified FJC model. More generally, the multiscale approach (Fig. 1) may be followed with different bond models and different chain models as constitutive components of the interface model, and the kinetics of damage evolution may also be replaced by other rate equations based on different mechanisms.

To illustrate how the present interface model works under various loading conditions, we consider two simple examples in this section. First, subject to a constant traction (σ), the damage increases over time by Eq. (5.5), the chain force increases by Eq. (5.6), and the energy barrier decreases by Eq. (4.9). Eventually, the damage reaches 1, meaning that all the chains have been broken at the interface. Similar to creep and creep rupture, the opening of the interface increases over time and the time to rupture the interface depends on the traction, as shown in Fig. 5 and Fig. 6, respectively. Here, we normalize all quantities as: $\bar{\sigma} = \sigma/\sigma_0$ (with $\sigma_0 = N_0 k_B T/r_0$), $\bar{\delta} = \delta/(nr_0) = \lambda$, and $\bar{t} = nt/t_0$. With this normalization, the results only depend on two dimensionless parameters: $\bar{\sigma}$ and $\bar{\varepsilon}$, whereas the chain density (N_0) only affects the magnitude of the stress ($\sigma_0 = N_0 k_B T/r_0$) and the chain length (n) influences both the length scale (nr_0) and the time scale (t_0/n). Fig. 5a shows that, for each traction level, the damage first increases slowly and then accelerates towards 1. When the chain force reaches the maximum (f_{max}), the damage is: $D_{max} = 1 - \sigma/(N_0 f_{max})$, and the energy barrier becomes zero so that chain scission occurs instantaneously as indicated by the cross markers. Similarly, Fig. 5b shows that the opening displacement starts with an instantaneous value (with $D = 0$ and $\bar{f}(\bar{\delta}) = \bar{\sigma}$), then increases slowly over time, and accelerates to failure at the end, resembling the creep behavior. Increasing the traction increases the initial opening, expedites the damage evolution, and shortens the time to failure (t_f). Fig. 6 shows that the time to failure ($\bar{t}_f = nt_f/t_0$) decreases rapidly with the increasing traction, resembling the creep rupture behavior. Remarkably, the normalized time to failure varies over a wide range (~20 decades), from essentially infinitely long time at very low traction to almost instantaneous failure ($t_f \sim t_0$) at a high traction close to the theoretical limit ($\sigma_{max} = N_0 f_{max}$). In addition, the effect of the bond energy and temperature can be predicted

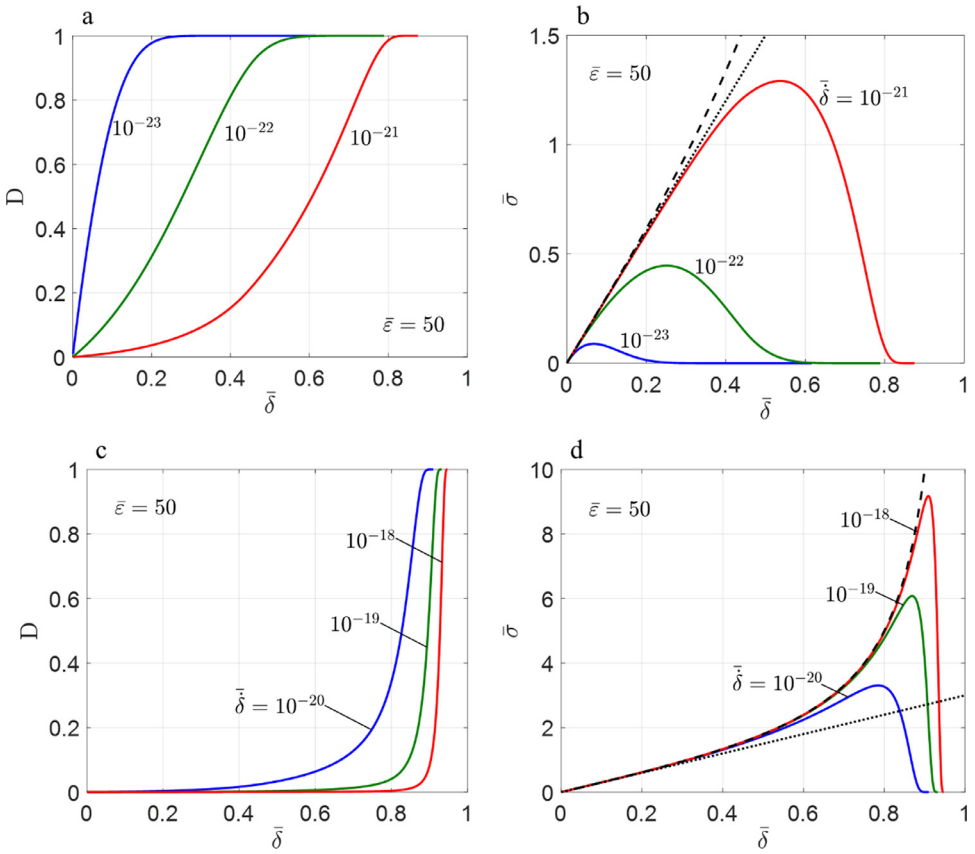

Fig. 7. Predicted damage evolution and traction-separation relations under constant separation rates with $\bar{\varepsilon} = 50$. (a-b) for relatively low separation rates, and (c-d) for relatively high separation rates. The dotted lines in (b) and (d) are for the linear Gaussian chain model with $\bar{\sigma} = 3\bar{\delta}$, and the dashed lines are for the nonlinear Langevin model with: $\bar{\sigma} = \mathcal{L}^{-1}(\bar{\delta})$, both independent of the separation rate with no damage ($D = 0$).

as well (Fig. 6). Notably, the temperature has a multitude of effects on the stress magnitude ($\sigma_0 = N_0 k_B T / r_0$), the time scale ($t_0 = \frac{\hbar}{k_B T}$), and the normalized bond energy ($\bar{\varepsilon} = \frac{\varepsilon_0}{k_B T}$). It can been seen that the trend for the time to failure in Fig. 6 is very similar to that in Fig. 4b for the normalized energy barrier, as a result of the thermally activated chain scission process.

As another common loading condition, we consider a monotonic loading with a constant separation rate ($\dot{\delta}$), i.e., $\delta(t) = \dot{\delta} t$, and normalize the separation rate as: $\dot{\bar{\delta}} = \dot{\delta} t_0 / (n^2 r_0)$. Here again, both the length scale ($n r_0$) and the time scale (t_0 / n) depend on the chain length (n). In this case, we obtain rate-dependent damage evolution and traction-separation relations, as shown in Fig. 7. At a relatively low separation rate, the damage evolution is significant even at relatively small separation (Fig. 7a), which leads to a decreasing stiffness in the traction-separation relation (Fig. 7b). The initial stiffness can be predicted by the linear Gaussian chain model, with $\bar{\sigma} = 3\bar{\delta}$ for $D = 0$. Thus, the dimensional stiffness for the interface is: $K_0 = \frac{3 N_0 k_B T}{n r_0^2}$, independent of the separate rate. With continual increase in damage, the traction decreases after a peak traction and becomes zero when the interface is fully damaged ($D = 1$). The softening part of the traction-separation relation is gradual at a low separation rate but becomes steeper as the separation rate increases. For a relatively high separation rate, the damage remains low until the separation is relatively large (Fig. 7c), which leads to a stiffening traction-separation relation (Fig. 7d), following the nonlinear Langevin mode with $\bar{\sigma} = \mathcal{L}^{-1}(\bar{\delta})$ (dashed lines). As the normalized separation ($\bar{\delta}$) or equivalently the chain stretch ($\lambda = \bar{\delta}$) approaches 1, the damage increases rapidly, leading to a peak traction followed by a steep softening in the traction-separation relation. Therefore, the rate-dependent damage evolution leads to two types of traction-separation relations (Figs. 7b and 7d) depending on the separation rate.

The key parameters for an interfacial traction-separation relation typically include: the initial stiffness (K_0), the peak traction or strength (σ_p), the maximum separation (δ_f), and the work of separation or toughness ($\Gamma = \int_0^{\delta_f} \sigma \, d\delta$). In the present model, except for the initial stiffness, the other three parameters are rate dependent, increasing as the separation rate increases. As shown in Fig. 8, for each value of the normalized bond energy, both the strength and the toughness of the interface depend on the normalized separation rate, with two different regimes. For relatively low separation rates, both the strength and the toughness are relatively low but depend sensitively on the separation rate, varying by several orders of magnitude. In contrast, for relatively high separation rates, the rate dependence is less significant, typically within one order

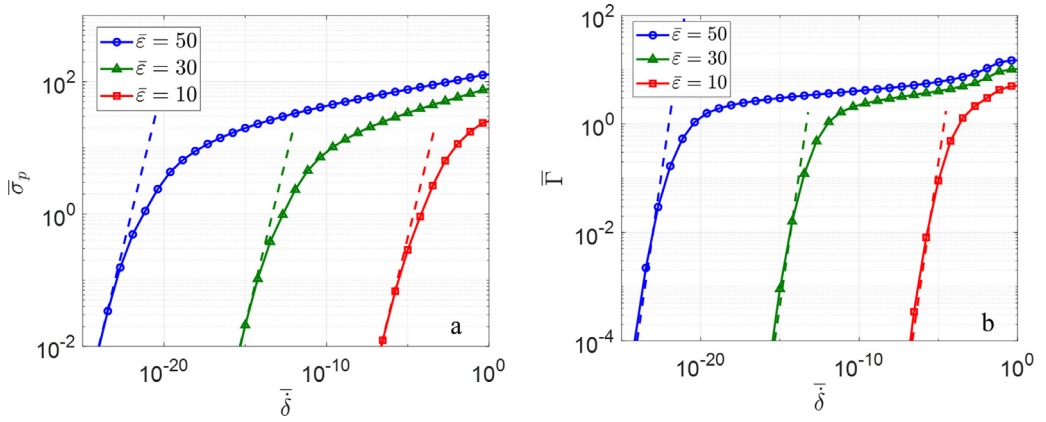

Fig. 8. (a) Normalized strength ($\bar{\sigma}_p = \sigma_p/\sigma_0$, with $\sigma_0 = N_0 k_B T/r_0$) and (b) toughness ($\bar{\Gamma} = \Gamma/\Gamma_0$, with $\Gamma_0 = N_0 n k_B T$) versus the normalized separation rate at different values of the normalized bond energy.

of magnitude. At very high separation rates ($\dot{\bar{\delta}} \to 1$), the strength approaches a theoretical limit set by the chain model as $\sigma_{max} = N_0 f_{max}$ and $\bar{\sigma}_p \to \bar{f}_{max}$, which is linearly proportional to the normalized bond energy. Correspondingly, the toughness approaches a theoretical limit following the force-stretch relation of the chain (Fig. 3b, up to the maximum force). We note that the toughness predicted by the present model is always less than that by the Lake-Thomas model for elastomers (Lake and Thomas, 1967). The latter assumes that all the bonds in the chains reach the rupture point simultaneously so that the toughness is simply $\Gamma_{LT} = nN_0\varepsilon_0$ and $\bar{\Gamma}_{LT} = \bar{\varepsilon}$ after normalization. As noted by Chaudhury (1999), the Lake-Thomas model can be understood only on the basis of the nonequilibrium aspects of bond dissociation. Considering the thermally activated chain scission mechanism in the present model, the energy barrier for chain scission drops to zero as the force reaches the maximum (f_{max}), at which point the chain breaks instantaneously. Therefore, the energy required to break each chain has an upper bound set by stretching the chain up to the maximum force, which does not include the softening part (unstable) of the chain response. Consequently, the theoretical limit for the chain scission energy is only a fraction of the total bond energy assumed in the Lake-Thomas model. Moreover, as a thermally activated process, the chains could break before the force reaches the maximum, thus lowering the toughness further as the separation rate decreases. Note that the toughness discussed here is strictly for the interface, without considering any other energy dissipation mechanisms in the bulk material. Apparently, an interface could be significantly toughened by energy dissipation in the surrounding materials via plasticity or other mechanisms (Hutchinson and Evans, 2000; Yang et al., 2020).

According to Fig. 8, both the strength and the toughness decreases as the bond energy decreases. The effect of temperature is more complicated as it simultaneously affects the normalized bond energy, the normalized separation rate, the normalized strength and toughness. It is found that the curves in Fig. 8 can be approximately collapsed by re-normalizing the separation rate as $\dot{\bar{\delta}}\exp(\bar{\varepsilon})$. For relatively low separation rates (i.e., $\dot{\bar{\delta}}\exp(\bar{\varepsilon}) < 1$), the normalized strength is linearly proportional to the separation rate and the toughness is proportional to the square of the separation rate, namely, $\bar{\sigma}_p \sim \dot{\bar{\delta}}\exp(\bar{\varepsilon})$ and $\bar{\Gamma} \sim \dot{\bar{\delta}}^2 \exp(2\bar{\varepsilon})$, as indicated by the dashed lines in Fig. 8.

6. Effect of statistically distributed chain lengths

The previous section considers thermally activated chain scission by assuming an identical chain length (n, the number of bonds per chain) for all the chains at the interface. More realistically, the chain length may be described by a statistical distribution (Itskov and Knyazeva, 2016; Li and Bouklas, 2020; Tehrani and Sarvestani, 2017; Verron and Gros, 2017).[2] In this section, we assume statistically distributed chain lengths as part of the multiscale interface model. We describe the initial distribution using a continuous chain density function, $\rho_0(n)$, which gives the number of chains per unit area with the chain lengths between n and $n + dn$. Then, the total number of chains per unit area is:

$$N_0 = \int \rho_0(n) dn, \tag{6.1}$$

where n may range from 1 to infinity or any specific limits ($n > 0$). Subject to a traction or separation, some of the chains break, and the number density of the intact chains evolve over time, i.e., $\rho(n) = (1 - D_n)\rho_0(n)$, where D_n is the damage

[2] In addition to the chain lengths, the chain orientations may also be statistically distributed. Here, we assume a single layer of parallel chains at the interface, leaving the effect of chain orientations for future studies.

parameter for the chains of n bonds and follows the same rate equation as in Eq. (5.5), namely

$$\frac{dD_n}{dt} = \frac{n}{t_0}(1 - D_n)\exp\left(-\frac{E_b}{k_B T}\right). \tag{6.2}$$

Assuming same separation (δ) for all the intact chains at the interface, the chain stretch ($\lambda_n = \delta/(nr_0)$) and the chain force ($f_n$) depend on the chain length. The traction at the interface is then

$$\sigma = \int (1 - D_n) f_n \rho_0(n) dn. \tag{6.3}$$

By Eqs. (6.2) and (6.3), along with Eq. (3.4) for the force-stretch relation of a chain and Eq. (4.9) for the energy barrier, the effect of statistically distributed chain lengths is accounted for in the multiscale interface model.

To be specific, we assume a normal distribution of the chain lengths as follows:

$$\rho_0(n) = \frac{N_0}{\sqrt{2\pi}\chi} \exp\left(-\frac{1}{2}\left(\frac{n - n_0}{\chi}\right)^2\right), \tag{6.4}$$

which is characterized by three parameters: the area chain density N_0, the average chain length n_0, and the standard deviation χ. Here, we have assumed that $n_0 - 3\chi > 1$ so that Eq. (6.1) holds for the range of chain lengths ($n > 1$).

As noted in Section 5, both the length scale and the time scale depend on the chain length. With statistically distributed chain lengths, the length and time scales are no longer uniquely defined for all the chains. Nevertheless, we may use the average chain length (n_0) to define a length scale ($n_0 r_0$) and a time scale (t_0/n_0). Then, following similar normalization as: $\bar{\sigma} = \sigma/\sigma_0$ (with $\sigma_0 = N_0 k_B T/r_0$), $\bar{\delta} = \delta/(n_0 r_0)$, and $\bar{t} = n_0 t/t_0$, the resulting equations have only two dimensionless parameters: $\bar{\varepsilon}$ and $\bar{\chi} = \chi/n_0$ (relative deviation), where $\bar{\chi} = 0$ for the case of a constant chain length as discussed in Section 5. If the interface is subject to a constant traction, the normalized creep-like behavior would depend on $\bar{\sigma}$, $\bar{\varepsilon}$, and $\bar{\chi}$, similar to Fig. 5 (where $\bar{\chi} = 0$). If the interface is subject to a constant separation rate, the normalized traction-separation relation would depend on the normalized separation rate, $\bar{\dot{\delta}} = \dot{\delta} t_0/(n_0^2 r_0)$, in addition to $\bar{\varepsilon}$ and $\bar{\chi}$, as shown in Fig. 9 for two different separation rates.

Fig. 9 (a-b) shows that the normalized traction-separation relation depends on the relative deviation $\bar{\chi}$. Compared to the case of a constant chain length ($\bar{\chi} = 0$), the initial interfacial stiffness increases slightly, the strength decreases, and the range of interactions increases, as $\bar{\chi}$ increases. In particular, the strength and range change more significantly under a relatively high separation rate (Fig. 9b). Fig. 9 (c-d) shows the evolving chain length distributions as the interfacial separation increases for $\bar{\chi} = 0.1$. While the initial distribution is the same, the evolution depends on the separation rate. At a relatively low separation rate (Fig. 9c), the chain length distribution appears to retain the shape of a normal distribution, but the peak shifts slowly to the right, indicating that the shorter chains break faster. In contrast, at a high separation rate (Fig. 9d), the chain length distribution becomes highly distorted, with the shorter chains breaking much faster than the longer chains. Evidently, the fast breaking of short chains leads to a reduced strength of the interface, whereas the presence of long chains extends the range of interactions.

Since the rate of chain scission varies with the chain length, the damage parameters evolve at different rates for different chain lengths. At the interface level, we define an overall damage parameter as: $D = 1 - \frac{N}{N_0}$, where N is the number of intact chains (regardless of the chain length) and can be calculated as

$$N = \int (1 - D_n)\rho_0(n) dn. \tag{6.5}$$

As shown in Fig. 9 (e-f), the evolution of the interfacial damage parameter depends on the relative deviation of the chain lengths as well as the separation rate. Compared to the case of a constant chain length ($\bar{\chi} = 0$), the interfacial damage grows faster at relatively low separations, due to breaking of the shorter chains. Then, the damage evolution becomes slower at large separations, due to the presence of longer chains. The effect is more significant for the higher separation rate, where the damage grows abruptly for the case of a constant chain length ($\bar{\chi} = 0$) but becomes more gradual with the statistically distributed chain lengths ($\bar{\chi} > 0$). Therefore, in the present model, the chain length distribution has a profound influence on the damage evolution and the traction-separation relation of the interface.

Three key parameters of the interfacial traction-separation relation can be predicted by the present model. First, the initial stiffness of the interface is independent of the separation rate but depends on the chain length distribution as

$$K_0 = \frac{3k_B T}{r_0^2} \int \frac{\rho_0(n)}{n} dn = \frac{3N_0 k_B T}{n_0 r_0^2} \bar{K}_0(\bar{\chi}), \tag{6.6}$$

where

$$\bar{K}_0(\bar{\chi}) = \frac{1}{\sqrt{2\pi}\bar{\chi}} \int \frac{1}{\bar{n}} \exp\left(-\frac{1}{2}\left(\frac{\bar{n} - 1}{\bar{\chi}}\right)^2\right) d\bar{n}. \tag{6.7}$$

As shown in Fig. 10a, $\bar{K}_0 = 1$ for the case of a constant chain length ($\bar{\chi} = 0$) but increases slightly with increasing $\bar{\chi}$. Next, the peak traction as the interfacial strength is shown in Fig. 10b as a function of $\bar{\chi}$ at different separation rates. By integrating the traction-separation relation, we obtain the interfacial toughness ($\Gamma = \int_0^{\delta_f} \sigma d\delta$), as shown in Fig. 10c. Interestingly,

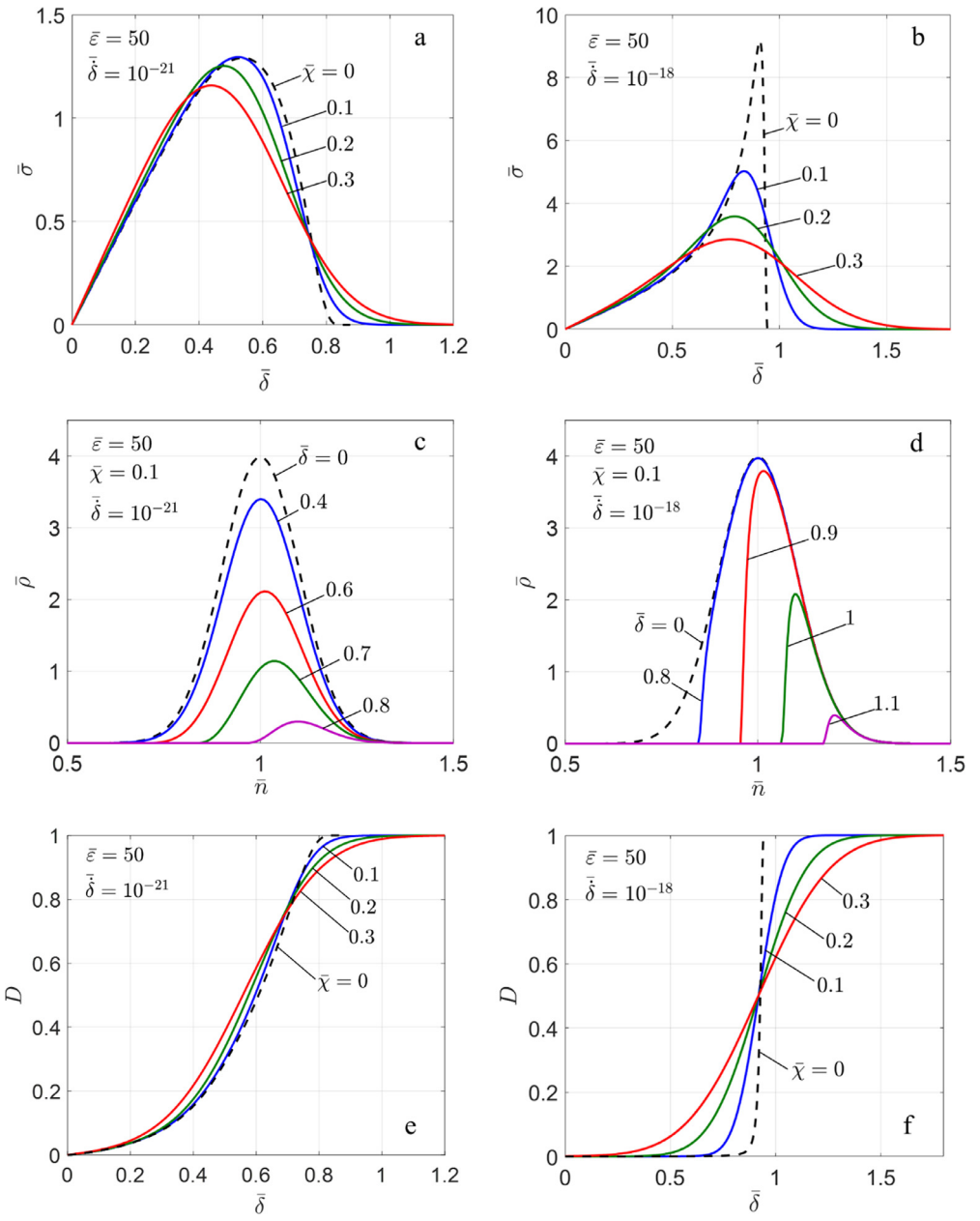

Fig. 9. Normalized traction-separation relations (a-b), chain length distributions (c-d), and damage evolution (e-f) under a constant separation rate. (a,c,e) for a relatively low separation rate, while (b,d,f) for a high separation rate.

while the interfacial strength may change significantly with the chain length distribution, especially at high separation rates, the interfacial toughness is less sensitive to the chain length distribution. Overall, both the strength and toughness decrease with increasing relative deviation, but the range of interactions increases, partly compensating for the decreasing strength so that the toughness does not change as much. This prediction appears to be consistent with experiments, where measurements of the interfacial toughness (or adhesion energy) are often commensurate among different methods or specimens, but the traction-separation relations could vary, which may be partly due to the statistical distributions of the chain lengths varying from specimen to specimen.

7. Specimen level: double cantilever beam experiments

In this section, the multiscale interface model formulated in the previous sections (Secs. 2-6) is implemented to simulate and compare with the rate-dependent fracture of an epoxy/silicon interface in double cantilever beam experiments. For nu-

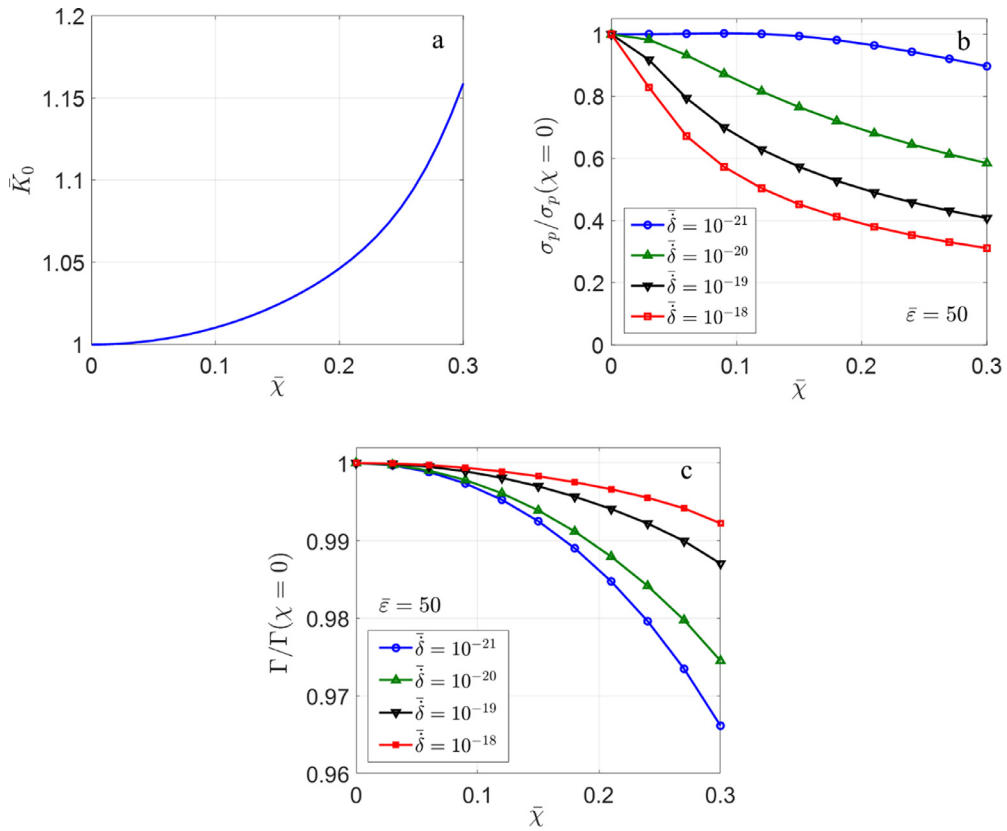

Fig. 10. Effects of the relative deviation in statistically distributed chain lengths on the predicted interfacial properties: (a) the initial stiffness, (b) the strength, and (c) the toughness, all normalized with respect to the corresponding properties for the case of a constant chain length ($\bar{\chi}=0$).

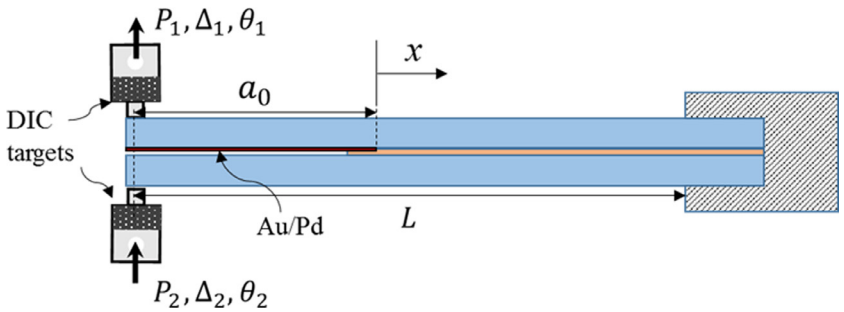

Fig. 11. Schematic of a double cantilever beam specimen subject to a dual-actuator loading.

merical simulations by the finite element method, the interface model is implemented as an user-defined interface (UINTER) subroutine in ABAQUS (see details in Appendix), which is then used to define the surface interactions between silicon and epoxy in the finite element analysis of the double cantilever beam experiments.

The specimen (Fig. 11) consists of two silicon beams as adherends and a layer of epoxy (EP 30, MasterBond Inc.) as the adhesive. Each silicon beam has the dimensions: $L=38$ mm (length), $b=5$ mm (width), and $h=1$ mm (thickness). The epoxy layer has a thickness of about 40 μm and a length of about 26 mm, leaving an initial crack of length $a_0 \approx 12$ mm. To help initiating an interfacial crack growth between silicon and epoxy, we coated a thin layer of Au/Pd (~15 nm thick) on part of the surface of the upper silicon beam, noting that the adhesion is relatively weak between the Au/Pd layer and the epoxy. The length of the Au/Pd coating was measured as the initial crack length (a_0) and listed in Table I for all specimens. More details about the specimen preparation can be found in a previous work (Yang et al., 2019). In the subsequent analysis, both silicon and epoxy are treated as linearly elastic with a Young's modulus and Poisson's rate, ($E=130$ GPa, $\nu=0.22$) for silicon and ($E_e=2.4$ GPa, $\nu_e=0.4$) for the epoxy. An independent measurement (Yang, 2020) found that the yield strength

Table I
Parameters for the experiments at different separation rates.

$\dot{\Delta}$ (mm/s)	a_0 (mm)	$\dot{\delta}^*$ (μm/s)	J_{ss} (J/m^2)	K_0 ($\times 10^{12}$ N/m^3)	σ_p (MPa)
0.625	12.13	11.46	11.5	8.8	11.6
0.125	12.10	2.18	8.8	9.8	9.2
0.025	12.34	0.44	6.2	7.8	6.1
0.005	12.19	0.083	2.1	10.2	3.0
0.001	12.10	0.018	1.2	9.4	1.8

of the epoxy (~ 30 MPa) is greater than the strength of the epoxy/silicon interface (< 12 MPa), thereby justifying the linearly elastic assumption.

The double cantilever beam experiments were conducted in a dual-actuator loading device (Yang, 2020). The direct measurements include the opening displacements (Δ_i), forces (P_i), and rotation angles (θ_i), all at the opening end of the specimen, where $i = 1, 2$ denotes the upper and lower beams, respectively. In particular, the rotation angles were measured by digital image correlation (DIC). While the dual-actuator loading device was designed for fracture experiments with arbitrary mode mix (Yang, 2020), symmetric loading conditions ($\Delta_2 = -\Delta_1$ and $P_2 = -P_1$) were maintained for all specimens in this study in order to ensure predominantly mode-I fracture of the interface. The effect of mode mix on rate-dependent interfacial fracture will be examined elsewhere (Yang et al., preparation). Here, the end opening ($\Delta = 2\Delta_1$) was controlled with a constant rate ($\dot{\Delta}$) for each specimen, as listed in Table I.

Following the method proposed by (Wu et al., 2019), the crack tip opening displacement (δ^*) and the normal component of J-integral (J_1, the energy release rate) can be obtained for the symmetric double cantilever beam specimen as

$$\delta^* = 2\Delta_1 + \frac{P_1 a_0^3}{3\bar{E}I} - 2a_0\theta_1, \tag{7.1}$$

$$J_1 = 2P_1\theta_1/b\ , \tag{7.2}$$

where $\bar{E} = E/(1-\nu^2)$ is the plane-strain modulus of silicon and $I = bh^3/12$. Then, the normal traction at the initial crack tip can be determined approximately as

$$\sigma^* = \partial J_1/\partial\delta^*. \tag{7.3}$$

We note that Eqs. (7.1-7.3) were derived from a linearly elastic beam analysis with the two silicon beams interacting via a traction-separation relation that is unknown *a priori* (Wu et al., 2019). The presence of a thin epoxy layer is ignored in this analysis.

By measuring a_0, Δ_1, P_1, and θ_1, we obtained from Eqs. (7.1-7.3) the crack tip displacement (δ^*), the J-integral (J_1), and then the traction-separation relation, $\sigma^*(\delta^*)$, at the initial crack tip. Fig. 12 (a-d) shows the force-displacement ($P_1 - \Delta_1$) curves, δ^* versus Δ_1, J_1 versus δ^*, and the traction-separation relations, respectively. For each specimen, both the force and the crack tip displacement first increased linearly with increasing Δ_1, and then the force decreased after a peak and the crack tip displacements increased at a much faster rate. Initiation of the crack growth was indicated by the deviation from the initially linear responses. Thus, the local separation rate at the initial crack tip ($\dot{\delta}^*$) was proportional to but much smaller than the applied separation rate ($\dot{\Delta}$) at the loading point before the crack growth was initiated, after which the local separation rate increased rapidly and was no longer a constant. The J-integral in Fig. 12c first increased and then approached a plateau value as the steady-state energy release rate (J_{ss}), which is clearly rate dependent. To extract the traction-separation relations by Eq. (7.3), the J-integral in Fig. 12c was fitted by continuous functions shown as dashed lines. The obtained traction-separation relations are rate dependent as shown in Fig. 12d, typically with an initial stiffness (K_0) for the linear portion and a peak traction (σ_p) followed by a softening portion towards zero traction. The values of J_{ss}, K_0 and σ_p thus obtained for the five specimens are listed in Table I along with the local separation rates $\dot{\delta}^*$ (Fig. 12b, for the linear part only). Notably, both J_{ss} and σ_p increased with increasing separation rate, whereas K_0 did not exhibit a clear rate dependence. Similar results were reported in our previous work with more specimens (Yang et al., 2019).

The measured load-displacement curves are typically linear before crack growth (Fig. 12a), based on which we can estimate the initial stiffness (K_0) of the interface using the beam-on-elastic-foundation model (Gowrishankar et al., 2012) as:

$$P_1 = \frac{3\bar{E}I\Delta_1}{a^3}\left(1 + \frac{3}{\xi a} + \frac{3}{(\xi a)^2} + \frac{3}{2(\xi a)^3}\right)^{-1}, \tag{7.4}$$

where $\xi = (6K_0/(\bar{E}h^3))^{1/4}$. With the initial crack length ($a = a_0$) and the measured slope of the load-displacement curves (Fig. 12a), the value of K_0 can be determined for each specimen, which turned out to be nearly identical to those obtained from the initial slope in the extracted traction-separation relations (Fig. 12d). Furthermore, by the beam-on-elastic-foundation model, the local separation rate at the initial crack tip can be estimated as (Yang et al., 2019)

$$\dot{\delta}^* = \dot{\Delta}\left(\frac{2}{3}(1+\xi a)^2 + \frac{1}{3(1+\xi a)}\right)^{-1}, \tag{7.5}$$

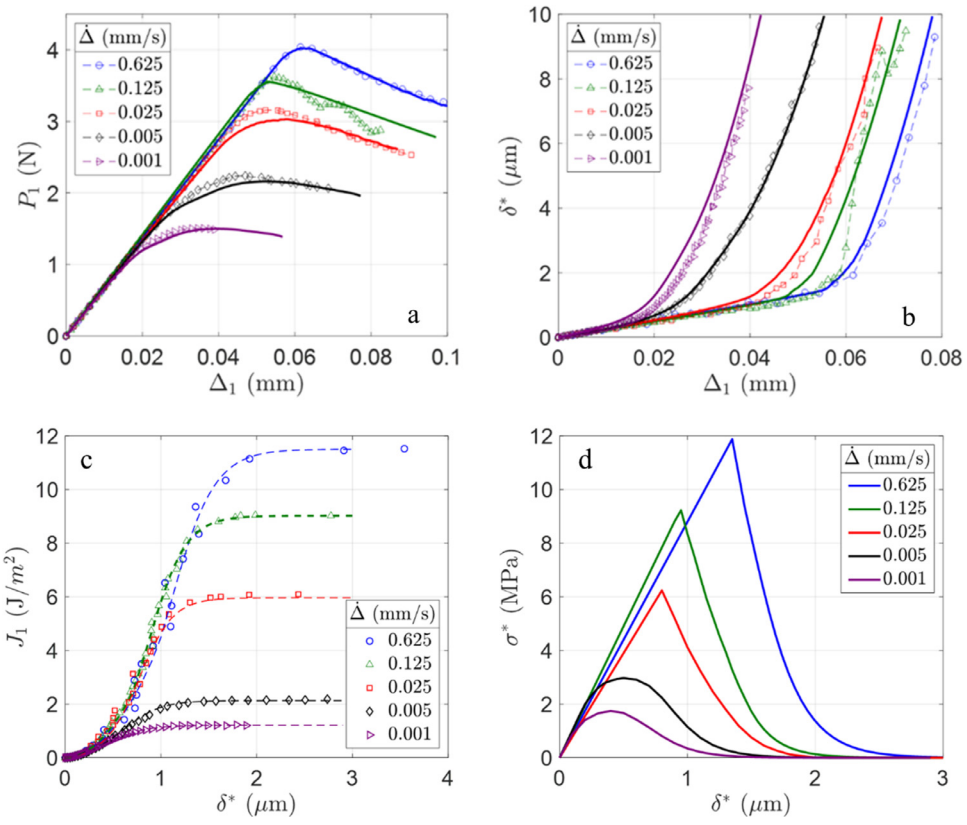

Fig. 12. (a) Force-displacement curves under different separation rates (measurements in symbols and simulations in solid lines); (b) Crack tip displacement versus the end displacement (symbols by Eq. (6.1) and solid lines by simulations); (c) J-integral versus crack tip displacement (data fitted by functions plotted as dashed lines); (d) Extracted traction-separation relations.

which is found to be consistent with the initial separation rate obtained by Eq. (7.1) or the linear part of Fig. 12b. We note that, unlike Eqs. (7.1-7.3), the beam-on-elastic-foundation model assumes that the two silicon beams interact via a linear traction-separation relation (Gowrishankar et al., 2012), thus limited to the linear portion of the interactions (before the initiation of crack growth).

Next, we determine the parameters in the multiscale interface model for the epoxy/silicon interface based on the double cantilever beam experiments. There are a total of six parameters in the present model: the bond energy (ε_0), bond length (r_0), initial chain density (N_0), average chain length (n_0), statistical deviation of chain lengths (χ), and the microscopic time scale (t_0). Among them, the time scale, as mentioned in Section 5, is set to be: $t_0 = \frac{\hbar}{k_B T} \sim 10^{-13}$ s for all specimens; here we take $k_B T = 0.0257$ eV for the room temperature (~25 °C). On the other hand, considering that the statistical distribution of chain lengths may vary from specimen to specimen, we allow different chain length deviations (χ) to be determined after the other parameters. Thus, we start by assuming $\chi = 0$ to determine four parameters: bond length (r_0), average chain length (n_0), chain density (N_0), and the bond energy (ε_0).

Recall that the peak stress and the toughness predicted by the present model (Fig. 8) are normalized by $\sigma_0 = N_0 k_B T / r_0$ and $\Gamma_0 = n_0 N_0 k_B T$, respectively. It is found that the two normalized quantities are closely correlated as shown in Fig. 13a, where the results from different combinations of the normalized separation rate and bond energy nearly collapse onto one curve.[3] This correlation enables us to determine the two quantities from the experiments as follows. A combination of the two normalized quantities can be related directly to the three dimensional quantities, namely

$$\bar{\Gamma}/\bar{\sigma}_p^2 = K_0 \Gamma / \left(3\sigma_p^2\right), \tag{7.6}$$

where $K_0 = 3N_0 k_B T/(n_0 r_0^2)$. With $\Gamma = J_{ss}$ and the values listed in Table I as the dimensional quantities extracted directly from the experiments, we obtain $\bar{\Gamma}/\bar{\sigma}_p^2$ for each specimen. For example, with $J_{ss} = 11.5$ J/m^2, $K_0 = 8.8 \times 10^{12}$ N/m^3, and $\sigma_p = 11.6$ MPa for the specimen with the highest separation rate ($\dot{\Delta} = 0.625$ mm/s), we obtain $\bar{\Gamma}/\bar{\sigma}_p^2 = 0.25$ by Eq. (7.6). For comparison with the model predictions in Fig. 13a, we draw a straight line in the log-log plot ($\bar{\Gamma}/\bar{\sigma}_p^2 = 0.25$), which

[3] This is because both the normalized strength and toughness approximately depend on one combination of the normalized separation rate and bond energy, $\bar{\delta}\exp(\bar{\varepsilon})$, especially for relatively slow separation rates ($\bar{\delta}\exp(\bar{\varepsilon}) < 1$), as noted in Section 5.

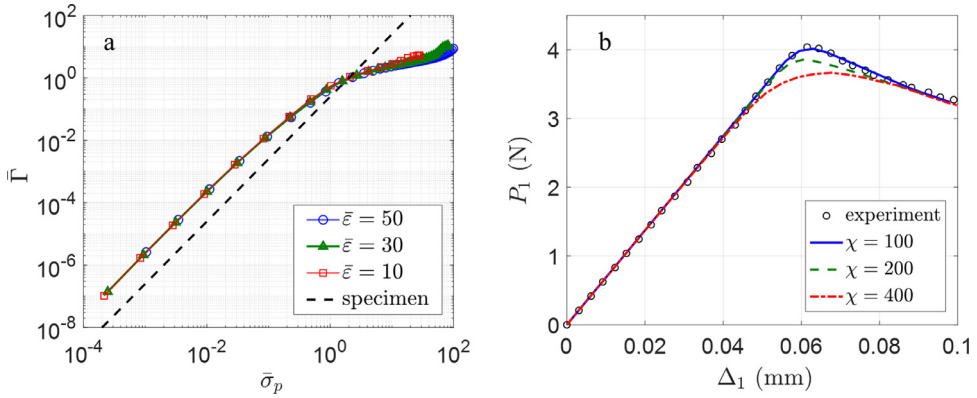

Fig. 13. (a) Correlation between the normalized toughness and strength predicted by the multiscale model, intersecting the dashed line with $\bar{\Gamma}/\bar{\sigma}_p^2 = 0.25$ for one specimen ($\dot{\Delta} = 0.625$ mm/s); (b) Comparison of the force-displacement curves from experiment ($\dot{\Delta} = 0.625$ mm/s) and numerical simulations with different deviations of the chain lengths.

Table II
Model parameters determined from experiments and used in numerical simulations.

$\dot{\Delta}$ (mm/s)	$\dot{\delta}^*$ (μm/s)	t_0 (s)	r_0 (nm)	n_0	N_0 ($\times 10^{17}$ m^{-2})	ε_0 (eV)	χ
0.625	11.46	10^{-13}	0.5	4008	7.37	1.00	100
0.125	2.18			3877	7.41	1.03	50
0.025	0.44			4065	6.41	1.06	50
0.005	0.083			4262	9.29	1.05	400
0.001	0.018			4560	8.63	1.05	450
Average				4154	7.82	1.04	210

intersects with the predicted curve at one point with particular values of $\bar{\Gamma}$ and $\bar{\sigma}_p$, $\bar{\Gamma} = 0.94$ and $\bar{\sigma}_p = 1.94$ for this specimen. Then, with $\Gamma = J_{ss} = 11.5$ J/m^2 and $\sigma_p = 11.6$ MPa, we obtain that $\Gamma_0 = 12.23$ J/m^2 and $\sigma_0 = 5.98$ MPa. With these values, we obtain $n_0 r_0 = \Gamma_0/\sigma_0 = 2.004$ μm and $\frac{N_0}{r_0} = \frac{\sigma_0}{k_B T} = 1.47 \times 10^{23}$ m^{-3}. To continue without additional measurements, we assume a constant bond length for all specimens in this work as: $r_0 = 0.5$ nm. Apparently, it is challenging (if not impossible) to determine this microscopic quantity solely based on macroscopic measurements. Nevertheless, with the constant bond length, we obtain $n_0 = 4008$ and $N_0 = 7.37 \times 10^{17}$ m^{-2} for this specimen ($\dot{\Delta} = 0.625$ mm/s). Hence, the local separation rate of 11.46 μm/s at the initial crack tip for this specimen corresponds to a normalized separation rate, $\bar{\dot{\delta}} = \dot{\delta} t_0/(n_0^2 r_0) = 1.43 \times 10^{-16}$, which is combined with the normalized toughness ($\bar{\Gamma} = 0.94$) to determine the bond energy (Fig. 8b), yielding a value of $\varepsilon_0 \sim 1.0$ eV ($\bar{\varepsilon} = 38.9$). Finally, to determine the statistical deviation of chain lengths (χ), we note that a small relative deviation ($\chi/n_0 < 0.1$) could be used to improve the agreement between the numerical simulations and the experiments (see Fig. 13b) without significantly altering the key properties of the interface (see Fig. 10). In particular, Fig. 13b shows that, with increasing χ, the peak force in the simulated load-displacement curve decreases and the transition from linear increasing to decreasing becomes more gradual. Following the same procedure, the model parameters are obtained for the five specimens as listed in Table II.

The extracted model parameters for the five specimens provide a consistent picture of the epoxy/silicon interface, with an average chain length of $n_0 = 4154$, an areal chain density of $N_0 = 7.82 \times 10^{17}$ m^{-2}, and an average bond energy of $\varepsilon_0 = 1.04$ eV. The statistical deviations of the chain lengths are relatively small ($\chi/n_0 < 0.1$) for each specimen, but could vary considerably from specimen to specimen. The areal chain density appears to be reasonable with an area of around 1 nm^2 per chain. The value of the bond energy is also quite reasonable, although it is lower than the typical values associated with covalent bonds such as Si-C and C–C bonds (~4.35 and 3.6 eV). We note that the molecular structure at the epoxy/silicon interface is likely different from the bulk epoxy, and further studies are needed to validate these parameters.

With the model parameters in Table II, we simulate the double cantilever beam experiments by the finite element method using ABAQUS. The finite element model consists of two silicon beams and an epoxy layer as shown schematically in Fig. 11, where the interactions between the epoxy and the upper silicon beam are described by the user-defined interface (UINTER) subroutine following the implementation of the rate-dependent cohesive zone model (see Appendix for details). The numerical results are compared to the experiments in Fig. 12 (a and b) in terms of the force-displacement curves and the opening displacements at the initial crack tip, respectively. Overall, the agreement is satisfactory for all five specimens. Notably, the simulated traction-separation relation varies along the interface because it depends on the local separation rate and history. As shown in Fig. 14a, both the strength and toughness are lower for the traction-separation relation at the initial crack tip, compared to those at the steady state ($x = 4.5$ mm). As the crack grows, the traction-separation relation eventually reaches a steady state at the new crack tip. This is in contrast with the common assumption that the

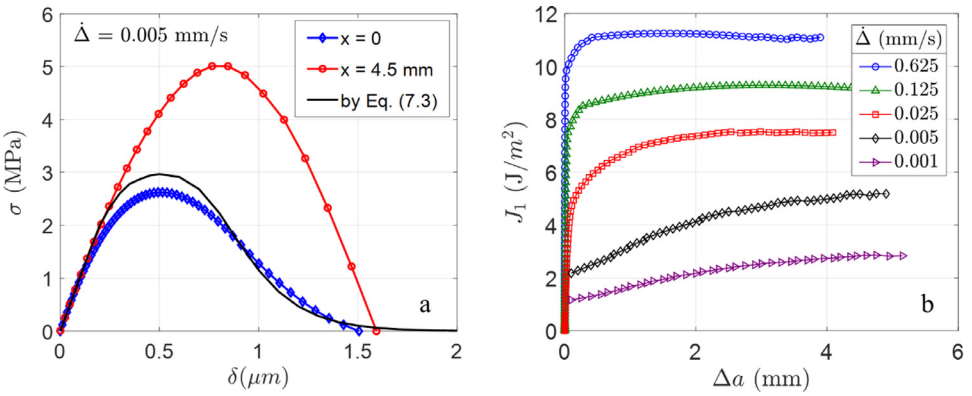

Fig. 14. (a) Simulated traction-separation relations at the initial crack tip ($x = 0$) and the steady state ($x = 4.5$ mm) in one specimen, in comparison to that obtained directly by Eq. (7.3); (b) Simulated fracture resistance curves for the double cantilever beam experiments.

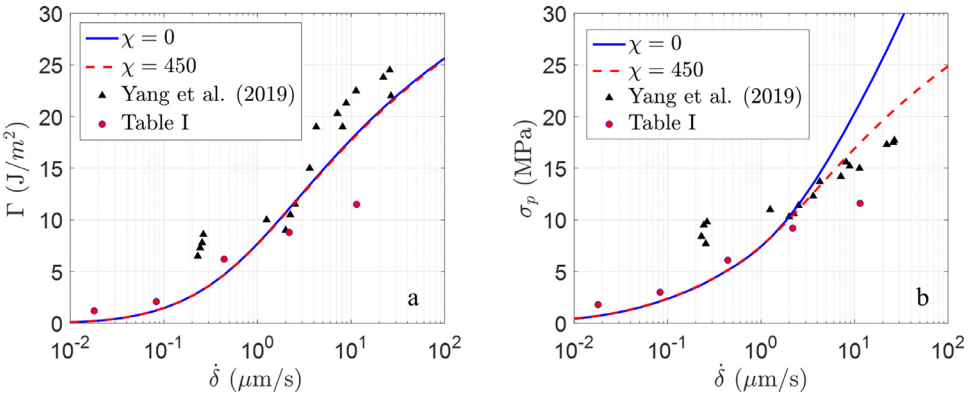

Fig. 15. Rate-dependent fracture toughness (a) and strength (b) of the silicon/epoxy interface predicted by the multiscale interface model, in comparison with the values extracted directly from the double cantilever beam experiments (Table I) and from the previous work (Yang et al., (2019).

same traction-separation relation can be used to describe the fracture processes of the interface as the crack grows. In fact, such an assumption was used to derive Eq. (7.2) for the J-integral and Eq. (7.3) (Wu et al., 2019). However, in the rate-dependent cohesive zone model, Eq. (7.3) is generally incorrect, and the J-integral must be calculated by definition with a contour enclosing the interface from the initial crack tip to the clamped end, namely

$$J_1 = \int_0^{L-a_0} \sigma \frac{\partial \delta}{\partial x} dx, \tag{7.7}$$

where $x = 0$ at the initial crack tip (Fig. 11). By Eq. (7.7), as the crack grows ($\Delta a > 0$), the J-integral increases and reaches a steady state value (Fig. 14b), a typical behavior for a fracture resistance curve (R-curve). Evidently, the J-integral for crack initiation corresponds to the traction-separation relation at the initial crack tip, and the steady-state J-integral corresponds to the traction-separation relation at a location ahead of the initial crack tip. For comparison, the traction-separation relation obtained by Eq. (7.3) is close to the crack-tip behavior (Fig. 14a), but underestimates the strength and toughness at the steady state. Moreover, it can be seen from Fig. 14b that it takes more crack growth (Δa) to reach the steady state for a lower separation rate, which is a reflection of the more gradual softening in the traction-separation relation at the lower rate (see Fig. 7) and correspondingly a relatively larger cohesive zone in the steady state.

Using the average values of the extracted model parameters (Table II), we can predict the rate-dependent properties of the epoxy/silicon interface, as shown in Fig. 15. Here, the toughness and strength are plotted as functions of the local separation rate (assumed to be a constant). The statistical deviation of the chain lengths is taken to be zero or 450 as the lower/upper bounds among the specimens. Consistent with Fig. 10, it is found that such a chain length deviation has a minimal effect on the interfacial toughness over a wide range of the separation rate (Fig. 15a). The effect on the interfacial strength is appreciable for relatively high separation rates, with a lower strength due to the statistical deviation of chain lengths. The predicted toughness and strength are compared to those extracted directly from the double cantilever beam experiments including those in a previous work (Yang et al., 2019). While the agreement appears to be reasonable, it is noted that the local separation rate was not a constant in the experiments except for the initially linear response. Moreover, in the previous work (Yang et al., 2019), these properties were extracted based on the beam-on-elastic foundation model assuming a linear traction-separation relation for the interface. In contrast, the properties in Table I were extracted without assuming

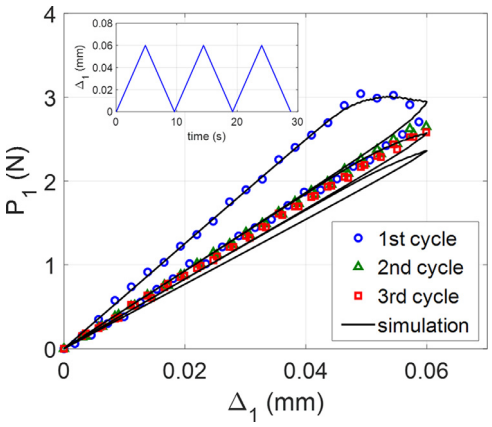

Fig. 16. Force-displacement of a double cantilever beam specimen under cyclic loading, comparing measurements (symbols) and simulation (solid lines). Inset shows the loading history.

a specific traction-separation relation but assuming that the relation is the same everywhere along the interface. Neither is exactly the case for the rate-dependent cohesive zone model, but may be considered as reasonable approximations for a direct method to extract the traction-separation relations from the double cantilever beam experiments.

The multiscale interface model, once calibrated by the experiments with the model parameters (Table II), can be used to predict fracture of the same interface under various conditions including monotonic and cyclic loadings, where the local separation rate may vary in time and location. Fig. 16 shows an example with a double cantilever beam specimen subject to a cyclic loading. Using the parameters for $\dot{\Delta} = 0.025$ mm/s in Table II, the numerical simulation agrees with the measurement very well for the first cycle, but appears to overestimate the amount of crack growth or damage evolution in the subsequent cycles. One possible reason may be due to healing, which has been ignored in the present model. As discussed in Section 4, healing is possible under displacement control, which would add a positive term to the right hand side of Eq. (5.3) for the chain survival probability and then a negative term to Eq. (5.5) or (6.2) for the damage evolution. The effect of healing could be an interesting and relevant feature for polymeric interfaces, which is left for future studies.

8. Summary

This paper presents a multiscale, mechanism-based cohesive zone model for rate-dependent fracture of polymer interfaces. The model relates the interfacial properties (i.e., stiffness, strength and toughness) to the molecular structures of the interface in terms of the bond energy, bond length, chain length, areal chain density, and statistical deviation of chain lengths. While the Lennard-Jones potential energy is adopted at the bond level to describe bond stretching, other bond models can be used as part of the multiscale model as well. To account for the configurational entropy of long molecular chains and to allow bond stretching (and breaking), a modified freely jointed chain model is proposed at the chain level. Again, other chain models may also be employed as part of the multiscale model. Next, a kinetic chain scission mechanism is modeled as a thermally activated process, with a microscopic time scale at the root of the rate-dependent behaviors and an energy barrier depending nonlinearly on the force. With a large number of identical chains at the interface level, the survival probability of the chains is related to the damage parameter of the interface, and the traction-separation relation can be predicted under various loading conditions. For a constant separation rate in particular, both the strength and toughness increase with the increasing rate, while the stiffness is rate independent. Furthermore, the statistical distributions of the chain lengths at the interface are considered by assuming a normal distribution. The relative deviation of the chain length could decrease the strength but increase the range of interactions, with a minimal effect on the toughness.

To compare with experiments, the multiscale cohesive zone model is implemented as a user-defined interface (UINTER) in ABAQUS and then used to simulate the rate-dependent fracture of an epoxy/silicon interface in double cantilever beam experiments. With the model parameters extracted from the experiments, the numerical simulations show good agreement with the direct measurements. Moreover, the model parameters extracted from different specimens at different separation rates provide a consistent description of the molecular structures at the interface, which may be used to predict the interfacial fracture under various conditions including monotonic and cyclic loadings. Future studies may consider additional effects such as healing within the same framework of the multiscale cohesive zone model.

Declaration of Competing Interest

The authors declare that they have no known competing financial interests or personal relationships that could have appeared to influence the work reported in this paper.

Acknowledgments

The authors gratefully acknowledge the financial support of this work by the Semiconductor Research Corporation (SRC Task ID: 2886.001).

Appendix: Finite element implementation

A two-dimensional, tri-layer finite element model was constructed in ABAQUS to simulate the double cantilever beam experiments (Fig. 11). Both the silicon beams and the epoxy layer were modeled by plane-strain quadrilateral elements (CPE8), with linearly elastic properties ($E = 130$ GPa and $\nu = 0.22$ for silicon; $E_e = 2.4$ GPa and $\nu_e = 0.4$ for the epoxy). The epoxy layer was tied to the bottom silicon beam, while the interface between the epoxy and the upper silicon beam was modeled by surface-to-surface interactions between a master (silicon) and a slave (epoxy). The epoxy layer was densely meshed (with at least 10 elements in the thickness direction) to avoid being penetrated by the master surface. In this work, the rate-dependent cohesive zone model was implemented as a user-defined subroutine (UINTER) for the interactions between the master-slave surface nodes. Unlike a typical rate-independent cohesive zone model, the present model does not prescribe a specific form of the traction-separation relation. Instead, the traction is calculated following the history of separation and damage evolution.

Given the relative displacements between the surface nodes, the tractions and the tangent stiffness are calculated by the user subroutine. In addition, the damage parameters must be updated based on the rate equation, Eq. (6.2). The implementation procedure is summarized as follows:

(1) With the input separation δ at the current step, the chain stretch $\lambda_n = \delta/(nr_0)$ is obtained for each chain length (n). Then, the corresponding bond stretch (λ_b) and the end force (f_n) are calculated by Eq. (3.3) and Eq. (3.4), respectively.
(2) Next, the energy barrier for chain scission is calculated as in Fig. 4. Alternatively, Eq. (4.9) may be used as an approximation for faster calculations.
(3) Then, integrate Eq. (6.2) over a time step to update the damage parameters (D_n) for each chain length. The damage parameters from the previous step are input as state variables.
(4) With the chain forces (f_n) and the updated damage parameters (D_n), calculate the traction by Eq. (6.3). The tangent stiffness $\partial\sigma/\partial\delta$ is calculated by numerical differentiation, with the tractions and separations at the current and the previous steps.

To speed up the computation, especially for solving Eq. (3.3) and Eq. (3.4) with the inverse Langevin function, we pre-solved these two equations for a range of the chain stretch (see Fig. 2) with relatively fine increments (e.g., $\delta\lambda/\lambda = 10^{-5}$) and save the results as a data file. Then we call the file to obtain the bond stretch and chain force for the current chain stretch by linear interpolation between the nearest stretches in the data file. Since both the bond stretch and the chain force increase monotonically with the chain stretch before reaching the peak force (see Fig. 3; the chain breaks instantaneously at the peak force), a simple binary search algorithm is employed to find the nearest chain stretches efficiently.

With statistically distributed chain lengths, the damage parameter for each chain length (D_n) has to be stored as the state variables (STATEV) at the current step and then used in the next step. This may require a large memory space for the numerical simulations, depending on the statistical distribution. In the present work, we consider the chain lengths within four times of the deviation ($n_0 - 4\chi \le n \le n_0 - 4\chi$) in a normal distribution. In this case, the required memory allocation increases with the increasing deviation (χ).

References

Ackbarow, T., Chen, X., Keten, S., Buehler, M.J., 2007. Hierarchies, multiple energy barriers, and robustness govern the fracture mechanics of alpha-helical and beta-sheet protein domains. Proc. Natl. Acad. Sci. U S A 104, 16410–16415.
Adjari, A., Brochard-Wyart, F., de Gennes, P.-G., Leibler, L., Viovy, J.-L., Rubinstein, M., 1994. Slippage of an entangled polymer melt on a grafted surface. Physica A 204, 17–39.
Alfano, G., Crisfield, M.A., 2001. Finite element interface models for the delamination analysis of laminated composites: mechanical and computational issues. Int. J. Numer. Methods Eng. 50, 1701–1736.
Barenblatt, G.I., 1959. The formation of equilibrium cracks during brittle fracture. General ideas and hypotheses. Axially-symmetric cracks.. J. Appl. Math. Mech. 23, 622–636.
Bell, G., 1978. Models for the specific adhesion of cells to cells. Science 200, 618–627.
Büyüköztürk, O., Buehler, M.J., Lau, D., Tuakta, C., 2011. Structural solution using molecular dynamics: fundamentals and a case study of epoxy-silica interface. Int. J. Solids Struct. 48, 2131–2140.
Chaudhury, M.K., 1999. Rate-dependent fracture at adhesive interface. J. Phys. Chem. B 103, 6562–6566.
Chen, H., Feng, X., Huang, Y., Huang, Y., Rogers, J.A., 2013. Experiments and viscoelastic analysis of peel test with patterned strips for applications to transfer printing. J. Mech. Phys. Solids 61, 1737–1752.
de Gennes, P.G., 1996. Soft Adhesives. Langmuir 12, 4497–4500.
Dugdale, D.S., 1960. Yielding of steel sheets containing slits. J. Mech. Phys. Solids 8, 100–104.
Evans, E., Ritchie, K., 1997. Dynamic strength of molecular adhesion bonds. Biophys. J. 72, 1541–1555.
Feng, X., Meitl, M.A., Bowen, A.M., Huang, Y., Nuzzo, R.G., Rogers, J.A., 2007. Competing fracture in kinetically controlled transfer printing. Langmuir 23, 12555–12560.
Freund, L.B., 2009. Characterizing the resistance generated by a molecular bond as it is forcibly separated. Proc. Natl. Acad. Sci. 106, 8818–8823.
Freund, L.B., 2014. Brittle crack growth modeled as the forced separation of chemical bonds within a K-field. J. Mech. Phys. Solids 64, 212–222.
Gent, A.N., Petrich, R.P., Tabor, D., 1969. Adhesion of viscoelastic materials to rigid substrates. Proc. R. Soc. Lond. A. Math. Phys. Sci. 310, 433–448.

Ghatak, A., Vorvolakos, K., She, H., Malotky, D.L., Chaudhury, M.K., 2000. Interfacial rate processes in adhesion and friction. J. Phys. Chem. B 104, 4018–4030.
Gowrishankar, S., Mei, H., Liechti, K.M., Huang, R., 2012. A comparison of direct and iterative methods for determining traction-separation relations. Int. J. Fract. 177, 109–128.
Hänggi, P., Talkner, P., Borkovec, M., 1990. Reaction-rate theory: fifty years after Kramers. Rev. Mod. Phys. 62, 251–341.
Hutchinson, J.W., Evans, A.G., 2000. Mechanics of materials: top-down approaches to fracture. Acta Mater. 48, 125–135.
Itskov, M., Knyazeva, A., 2016. A rubber elasticity and softening model based on chain length statistics. Int. J. Solids Struct. 80, 512–519.
Knauss, W.G., 2015. A review of fracture in viscoelastic materials. Int. J. Fract. 196, 99–146.
Knauss, W.G., Losi, G.U., 1993. Crack propagation in a nonlinearly viscoelastic solid with relevance to adhesive bond failure. J. Appl. Mech. 60, 793–801.
Kogan, L., Hui, C.Y., Ruina, A., 1996. Theory of Chain Pull-Out and Stability of Weak Polymer Interfaces. 1. Macromolecules 29, 4090–4100.
Kovalchick, C., Molinari, A., Ravichandran, G., 2013. Rate Dependent Adhesion Energy and Nonsteady Peeling of Inextensible Tapes. J. Appl. Mech. 81, 041016.
Kramers, H.A., 1940. Brownian motion in a field of force and the diffusion model of chemical reactions. Physica 7, 284–304.
Kuhn, W., Grün, F., 1942. Beziehungen zwischen elastischen Konstanten und Dehnungsdoppelbrechung hochelastischer Stoffe. Kolloid-Zeitschrift 101, 248–271.
Lake, G., Thomas, A., 1967. The strength of highly elastic materials. Proc. R. Soc. Lond. Series A. Math. Phys. Sci. 300, 108–119.
Landis, C.M., Pardoen, T., Hutchinson, J.W., 2000. Crack velocity dependent toughness in rate dependent materials. Mech. Mater. 32, 663–678.
Lavoie, S.R., Long, R., Tang, T., 2020. Modeling the mechanics of polymer chains with deformable and active bonds. J. Phys. Chem. B 124, 253–265.
Li, B., Bouklas, N., 2020. A variational phase-field model for brittle fracture in polydisperse elastomer networks. Int. J. Solids Struct. 182, 193–204.
Liechti, K.M., Wu, J.-D., 2001. Mixed-mode, time-dependent rubber/metal debonding. J. Mech. Phys. Solids 49, 1039–1072.
Makarov, D.E., 2015. Single Molecule Science: Physical Principles and Models. CRC Press, Boca Raton.
Makhecha, D.P., Kapania, R.K., Johnson, E.R., Dillard, D.A., Jacob, G.C., Starbuck, J.M., 2009. Rate-Dependent Cohesive Zone Modeling of Unstable Crack Growth in an Epoxy Adhesive. Mech. Adv. Mater. Struct. 16, 12–19.
Mao, Y., Talamini, B., Anand, L., 2017. Rupture of polymers by chain scission. Extreme Mech. Lett. 13, 17–24.
Marzi, S., Hesebeck, O., Brede, M., Kleiner, F., 2009. A Rate-Dependent Cohesive Zone Model for Adhesively Bonded Joints Loaded in Mode I. J. Adhes. Sci. Technol. 23, 881–898.
Meitl, M.A., Zhu, Z.-T., Kumar, V., Lee, K.J., Feng, X., Huang, Y.Y., Adesida, I., Nuzzo, R.G., Rogers, J.A., 2006. Transfer printing by kinetic control of adhesion to an elastomeric stamp. Nat. Mater. 5, 33–38.
Mohammed, I.K., Charalambides, M.N., Kinloch, A.J., 2016. Modeling the effect of rate and geometry on peeling and tack of pressure-sensitive adhesives. J. Non Newtonian Fluid Mech. 233, 85–94.
Na, S.R., Suk, J.W., Tao, L., Akinwande, D., Ruoff, R.S., Huang, R., Liechti, K.M., 2015. Selective mechanical transfer of graphene from seed copper foil using rate effects. ACS Nano 9, 1325–1335.
Neggers, J., Hoefnagels, J.P.M., Van Der Sluis, O., Geers, M.G.D., 2015. Multi-scale experimental analysis of rate dependent metal–elastomer interface mechanics. J. Mech. Phys. Solids 80, 26–36.
Pobelov, I.V., Lauritzen, K.P., Yoshida, K., Jensen, A., Mészáros, G., Jacobsen, K.W., Strange, M., Wandlowski, T., Solomon, G.C., 2017. Dynamic breaking of a single gold bond. Nat. Commun. 8, 15931.
Qian, J., Lin, J., Xu, G.-K., Lin, Y., Gao, H., 2017. Thermally assisted peeling of an elastic strip in adhesion with a substrate via molecular bonds. J. Mech. Phys. Solids 101, 197–208.
Raphael, E., De Gennes, P.G., 1992. Rubber-rubber adhesion with connector molecules. J. Phys. Chem. 96, 4002–4007.
Tehrani, M., Sarvestani, A., 2017. Effect of chain length distribution on mechanical behavior of polymeric networks. Eur. Polym. J. 87, 136–146.
Ungsuwarungsri, T., Knauss, W.G., 1987. The role of damage-softened material behavior in the fracture of composites and adhesives. Int. J. Fracture 35, 221–241.
Verron, E., Gros, A., 2017. An equal force theory for network models of soft materials with arbitrary molecular weight distribution. J. Mech. Phys. Solids 106, 176–190.
Wei, Y., 2014. A stochastic description on the traction-separation law of an interface with non-covalent bonding. J. Mech. Phys. Solids 70, 227–241.
Wiita, A.P., Ainavarapu, S.R.K., Huang, H.H., Fernandez, J.M., 2006. Force-dependent chemical kinetics of disulfide bond reduction observed with single–molecule techniques. Proc. Natl. Acad. Sci. 103, 7222–7227.
Wu, C., Huang, R., Liechti, K.M., 2019. Simultaneous extraction of tensile and shear interactions at interfaces. J. Mech. Phys. Solids 125, 225–254.
Xu, C., Siegmund, T., Ramani, K., 2003. Rate-dependent crack growth in adhesives: I. Modeling Approach. . Int. J. Adhesion Adhes. 23, 9–13.
Xu, C., Yang, T., Kang, Y., Li, Q., Xue, T., Liechti, K.M., Huang, R., Qiu, W., 2019. Rate-dependent decohesion modes in graphene-sandwiched interfaces. Adv. Mater. Interf. 6, 1901217.
Xu, D.B., Hui, C.Y., Kramer, E.J., Creton, C., 1991. A micromechanical model of crack growth along polymer interfaces. Mech. Mater. 11, 257–268.
Xu, X.P., Needleman, A., 1994. Numerical simulations of fast crack growth in brittle solids. J. Mech. Phys. Solids 42, 1397–1434.
Yang, J., Bai, R., Chen, B., Suo, Z., 2020. Hydrogel adhesion: a supramolecular synergy of chemistry, topology, and mechanics. Adv. Funct. Mater. 30, 1901693.
Yang, T., 2020. Rate-dependent fracture of a silicon/epoxy interface under mixed-mode loading conditions. PhD Dissertation, The University of Texas at Austin.
Yang, T., Huang, R., Liechti, K.M., 2020 In preparation. Rate dependent fracture along a silicon/epoxy interface under mixed-mode loading conditions.
Yang, T., Yang, X., Huang, R., Liechti, K.M., 2019. Rate-dependent traction-separation relations for a silicon/epoxy interface informed by experiments and bond rupture kinetics. J. Mech. Phys. Solids 131, 1–19.
Zhang, X., Mai, Y.-W., Jeffrey, R.G., 2003. A cohesive plastic and damage zone model for dynamic crack growth in rate-dependent materials. Int. J. Solids Struct. 40, 5819–5837.
Zhu, Y., Liechti, K.M., Ravi-Chandar, K., 2009. Direct extraction of rate-dependent traction-separation laws for polyurea/steel interfaces. Int. J. Solids and Structures 46, 31–51.
Zhurkov, S.N., 1965. Kinetic concept of the strength of solids. Int. J. Fract.Mech. 1, 311–323.